Deconvolution of FIGAERO-CIMS thermal desorption profiles using positive matrix factorisation to identify chemical and physical processes during particle evaporation

Angela Buchholz[1], Arttu Ylisirniö[1], Wei Huang[2], Claudia Mohr[3], Manjula Canagaratna[4], Douglas R. Worsnop[4], Siegfried Schobesberger[1], Annele Virtanen[1]

[1]Department of Applied Physics, University of Eastern Finland, Kuopio, Finland
[2]Institute of Meteorology and Climate Research, Karlsruhe Institute of Technology, Karlsruhe, Germany
[3]Department of Environmental Science and Analytical Chemistry, Stockholm University, Stockholm, Sweden
[4]Aerodyne Research Inc., Billerica, MA 08121-3976, USA

Abstract

Measurements of aerosol particles with a filter inlet for gases and aerosols (FIGAERO) together with a chemical ionisation mass spectrometer (CIMS) yield the overall chemical composition of the particle phase. In addition, the thermal desorption profiles obtained for each detected ion composition contain information about the volatility of the detected compounds, an important property to understand many physical properties like gas/particle partitioning. We coupled this thermal desorption method with isothermal evaporation prior to the sample collection to investigate the chemical composition changes during isothermal particle evaporation and particulate water driven chemical reactions in α-pinene SOA of three different oxidative states. The thermal desorption profiles of all detected elemental compositions were then analysed with positive matrix factorisation (PMF) to identify the drivers of the chemical composition changes observed during isothermal evaporation. The key to this analysis was to use the error matrix as a tool to weight the parts of the data carrying most information (i.e., the peak area of each thermogram) and to run PMF on a combined dataset of multiple thermograms from different experiments to enable direct comparison of the individual factors between separate measurements.

PMF was able to identify instrument background factors and separate them from the part of the data containing particle desorption information. Additionally, PMF allowed us to separate the direct desorption of compounds detected at a specific elemental composition from signals at the same composition stemming from thermal decomposition of thermally instable compounds of lower volatility. For each SOA type, 7 – 9 factors were needed to explain the observed thermogram behaviour. The contribution of the factors depended on the prior isothermal evaporation. Decreased contributions from the lowest desorption temperatures factors were observed with increasing isothermal evaporation time. Thus, the factors identified with PMF could be interpreted as volatility classes. The composition changes in the particles due to isothermal

evaporation could be attributed to the removal of volatile factors with very little change in the desorption profiles of the individual factors (i.e., in the respective temperatures of peak desorption, T_{max}). When aqueous phase reactions took place, PMF was able to identify a new factor which directly identified ions affected by the chemical processes.

We conducted PMF analysis of FIGAERO-CIMS thermal desorption data for the first time using laboratory generated SOA particles. But this method can be applied to e.g. ambient FIGAERO-CIMS measurements as well. There, it adds the information about particle volatility to that about the sources (such as biomass burning or oxidation of different precursors) or the type (e.g. hydrocarbon-like (HOA) or oxygenated organic aerosol (OOA)) of the organic aerosol particles. While the latter could also be obtained by PMF analysis of the mass spectra data integrated for each thermogram scan, only the analysis of the thermal desorption data can reveal information about volatility and at the same time identify the contribution of thermal decomposition to the overall signal.

1   Introduction

To understand the impact of secondary organic aerosol (SOA) on the earth's climate and human health, we need to know more about the chemical and physical properties of these particles and how they evolve with time in the atmosphere. The physical properties of SOA particles are controlled by the physical properties of their constituents and the interaction of the compounds in these complex mixtures. Volatility of SOA constituents is one of the defining characteristics of SOA particles as it plays a key role in understanding (and predicting) the partitioning behaviour of a compound between the gas and particle phase (Pankow, 1994a, 1994b; Pankow et al., 2001). Generally, whether a compound partitions into the particle phase is controlled by the saturation vapour pressure (volatility) of the involved compound, its concentrations, and the available condensation sink. In addition to that, particle phase processes also play an important role, especially when particle-phase compounds are partitioning back into the gas phase. In highly viscous or solid particles, mass transfer limitations exist that reduce the apparent particle volatility (Buchholz et al., 2019; Wilson et al., 2015; Yli-Juuti et al., 2017). The partitioning process gets complicated further by particle-phase chemical reactions. Accretion reactions can convert more volatile compounds into larger and heavier compounds thereby again changing the overall properties of the SOA particles (Herrmann, 2003; Kroll and Seinfeld, 2008). Particulate water plays a special role in these particle phase processes. On the one hand, it will act as a plasticiser, reducing the particle viscosity (Renbaum-Wolff et al., 2013; Virtanen et al., 2010) and thus reducing the mass transport limitation in the particles. These transport limitations are responsible for the reduced evaporation under dry conditions (Liu et al., 2016; Wilson et al., 2015; Yli-Juuti et al., 2017). On the other hand, the presence of an aqueous phase enables a wide range of chemical reactions with the potential of forming low volatility compounds via oligomerisation reactions (e.g. Surratt et al., 2007; Tolocka et al., 2004). Hydrolysis of labile bonds (e.g. peroxides or esters) is also possible, which would lead to more volatile products.

There are many challenges involved in trying to fully characterise SOA particles and their volatility. Already the sheer number of precursor compounds and their reaction products, which may contribute to the particle phase by forming new particles or condensing on existing ones, makes it almost impossible to fully characterise the chemical composition of SOA particles (Glasius and Goldstein, 2016; Goldstein and Galbally, 2007). However, the development of the filter inlet

5   for gases and aerosols (FIGAERO, Lopez-Hilfiker et al. (2014)) for the chemical ionisation mass spectrometer (CIMS) was a big step forward for the chemical characterisation of SOA particles as it provides more detailed information about the molecular composition and at the same time records the thermal desorption behaviour (thermogram) of each detected ion. Hence, in addition to composition information, FIGAERO measurements enable the determination of the volatility of SOA constituents as in an ideal case the peak desorption temperature (T_{max}, temperature at peak of ion thermogram) of

10   a single ion thermogram is correlated to the ion volatility expressed by its effective saturation vapour pressure, C_{sat}^* (Lopez-Hilfiker et al., 2014; Schobesberger et al., 2018). This relationship can be calibrated for a specific FIGAERO-CIMS setup and temperature ramp by measuring compounds with known volatilities, e.g. carboxylic acids (Lopez-Hilfiker et al., 2014) or polyethylene glycol (Bannan et al., 2019). Unfortunately, in most cases the data interpretation is more complicated as some compounds will not desorb from the FIGAERO filter at a temperature corresponding to their

15   volatility, but rather decompose at a lower temperature and the decomposition products will be detected in a mass spectrometer (D'Ambro et al., 2019; Lopez-Hilfiker et al., 2015; Stark et al., 2017; Wang and Hildebrandt Ruiz, 2018). The decomposition products may have the exact same sum formula as other constituents of the particles. Thus, only the shape of the ion thermogram may give a hint if an ion stems from desorption (typically sharp peak) or decomposition of one or several different larger compounds (typically broad peak or broad tailing on peak, Schobesberger et al., 2018).

20   Further complication for the interpretation of the T_{max} values arises from the presence of multiple isomers with different volatilities. Depending on how close the T_{max} values of the isomers are and the contribution of each isomer to the signal at this ion mass, the resulting ion thermogram may be multimodal, broadened or with considerable tailing/fronting.

To overcome the issues related to thermal decomposition, and further the interpretation of the ion thermograms, we utilised positive matrix factorization (PMF) in FIGAERO data interpretation. Traditionally, PMF has been used to analyse

25   complex mass spectra datasets mostly to identify the contribution of different sources to the total organic aerosol mass (Jimenez et al., 2009; Lanz et al., 2007; Ulbrich et al., 2009). But for PMF it does not matter if the "source" of a mass spectra signal is a real physical source (e.g. biomass burning, or traffic emissions) or if the source is particles collected on a filter being desorbed. PMF identifies the characteristic changes in the contribution of a source to the total signal, i.e. in the case of FIGAERO-CIMS data one or more compounds desorbing at a specific temperature range. In this study we

30   apply PMF for the first time in FIGAERO-CIMS data analysis to distinguish the direct desorption (controlled by C_{sat}^*) from the thermal decomposition of thermally labile compounds of lower volatility (controlled by the strength of the

weakest bond in the molecule). Further, we combine the FIGAERO-CIMS PMF analysis with the information gained from isothermal evaporation experiments where the particle composition evolves during the isothermal evaporation of the particles to understand processes controlling particle volatility.

2   Methodology

2.1   Dataset

The acquisition of the dataset investigated in this study was described in detail in Buchholz et al. (2019) and in the SI material. The schematic overview of the setup is shown in Figure 1. Briefly, three types of SOA were formed via combined ozonolysis and photooxidation of α-pinene in an oxidative flow reactor (OFR). They are characterised as low-, medium-, and highOC, based on their elemental composition (O:C ratio of 0.53, 0.69, and 0.96, respectively, derived from aerosol mass spectrometer data). A Nano differential mobility analyser (NanoDMA) was used to select a quasi-monodisperse particle distribution (electrical mobility diameter 80 nm) and at the same time dilute the surrounding gas phase by orders of magnitude, which initiates isothermal evaporation at the NanoDMA outlet. The monodisperse particles were then filled into a stainless-steel residence time chamber (RTC) to study their isothermal evaporation behaviour by measuring the particle size in 1 h intervals for up to 10 h. Two sets of evaporation experiments were conducted for each SOA type: dry (RH <2%) and wet (RH80%). To achieve the different RH conditions, only the RH of the sheath flow in the NanoDMA was adjusted, which controls the RH of the selected sample and in the RTC. The conditions of α-pinene SOA formation in the OFR were not changed. Between experiments the instruments, tubing, RTC, and OFR were flushed with particle-free, purified air or nitrogen.

The chemical composition of the particles was investigated directly after the size selection ("fresh" particles, t_{evap} = 0.25 h) and after 3 – 4 h of isothermal evaporation in the RTC ("RTC" particles, t_{evap} = 4 h) with a filter inlet for gases and aerosols (FIGAERO, Aerodyne Research Inc., Lopez-Hilfiker et al., 2014) sampling unit in combination with a chemical ionisation mass spectrometer (CIMS, Aerodyne Research Inc., Lee et al., 2014) using iodide as reagent ion. Note that the evaporation time of 0.25 h for the "fresh" sample does not stem from residence in the RTC but rather from the collection time on the filter (see SI section 1.1 for details). Due to this minimum evaporation time the FIGAERO-CIMS measurements will underestimate the contribution of volatile compounds in the particles as they leave the OFR.

The combined analysis of evaporation behaviour and FIGAERO-CIMS thermogram and composition information in Buchholz et al. (2019) revealed increasing average desorption temperatures with increasing O:C ratio of the particles while the overall particle volatility (measured by isothermal evaporation) decreased. The residual particles after isothermal evaporation in the RTC exhibited an increase in desorption temperature in all cases indicating that the more volatile species had left the particles. Under wet conditions, evaporation was enhanced due to lowering of particle

viscosity and thus kinetic transport limitations as described before (D'Ambro et al., 2018; Wilson et al., 2015; Yli-Juuti et al., 2017). But in the highOC case, strong indications for aqueous phase chemistry were found in the data, namely the shift of some ion thermograms to much higher desorption temperatures and a relative increase in low molecular weight (M_w) compounds. This dataset is thus perfect to test the performance of PMF with FIGAERO-CIMS data: Can PMF capture the evaporation behaviour and separate it from aqueous phase processes in the highOC case?

2.2 FIGAERO-CIMS measurements

It is necessary to understand the operation and data structure of FIGAERO-CIMS to comprehend the challenges of analysing this data with PMF. In the FIGAERO inlet, particles are collected on a PTFE filter. A gradually heated nitrogen gas flow evaporates increasingly less volatile compounds and transports them into the CIMS for detection. In the following, the resulting signal vs desorption temperature curves will be called ion thermogram for individual ions and total thermogram for the sum of all detected ions apart from the reagent ions. Each desorption cycle ("thermogram scan") consists of three parts: the particle collection, the linear increase of the desorption temperature (here, ~25 °C → ~190 °C in 15 min), and a "soak" period at the highest temperature (> 190 °C, 15 min). The soak period ensures that low volatility compounds have been removed from the FIGAERO filter before the next sample is collected. Note that only the part of the thermogram with a near linear increase in the desorption temperature can be used to derive volatility information. The relationship between a compound's desorption temperature, specifically T_{max}, and volatility (e.g. expressed as saturation vapour pressure) can be calibrated for a specific FIGAERO-CIMS setup and temperature ramp, e.g., by measuring polyethylene glycol aerosol with a range of molecular weights and volatilities (similar to the method described by Bannan et al. (2019)).

The raw FIGAERO-CIMS data was processed using tofTools, a MATLAB-based software package developed for analysing ToF-CIMS data (Junninen et al., 2010). The data was averaged to a 20 s time grid, and baseline correction was applied before the high-resolution mass spectra data was fitted. The filter blank measurements were processed in the same fashion as the collected samples. For the PMF analysis, we did not subtract the filter blank measurements but rather added the corresponding filter blank thermograms to the dataset to help with the identification the background factors, i.e., factors dominated by compounds from the instrument and/or filter background (more details on factor identification in section 3.1).

Due to sub-optimal settings in the instrument ion guidance unit, an atypically high amount of declustered ions (not containing the reagent ion iodide) was observed. This was discussed in detail in Buchholz et al. (2019). For this study, we will not make any assumptions about the declustering process and treat the iodide clusters and declustered ions as separate variables. However, this does not impact the application of PMF to the dataset and the validity of this method

for other datasets, as the variables (ions) are all treated independently in the model and variables with the same behaviour will be grouped into the same factor.

2.3 Positive matrix factorisation (PMF)

2.3.1 Working principles of PMF

5 Since its introduction by Paatero and Tapper (1994), PMF has been established as a useful tool to analyse long time series of mass spectra data mostly from ambient observations.

In the PMF model, it is assumed that the measured data can be expressed by the combination of an (unknown) number p of constant source profiles with varying concentrations over time (Ulbrich et al., 2009). This can be mathematically expressed as:

$$X = GF + E \tag{1}$$

X is a $m \times n$ matrix containing the measured mass spectra containing m rows of mass spectra ("observations") each averaged over 20 s of measurement time in the CIMS and n columns representing the time series of one specific ion. G is a $m \times p$ matrix containing the factor time series as columns. The rows of the $p \times n$ matrix F contain the factor mass spectra. Then the $m \times n$ matrix E contains the residuals between the measured data and the fitted values. No a priori

15 information about the values of G and F or the number of factors (p) is required, but the user has to decide which solution (i.e., how many factors) characterises the data best. To account for uncertainties in the measurement data, the PMF model weights the data points with their measurement error (S_{ij}). Values for G and F are constrained to be positive and iteratively found by minimising the quantity, Q, with a least square algorithm (Paatero and Tapper, 1994):

$$Q = \sum_{j=1}^{m} \sum_{i=1}^{n} \left(\frac{E_{ij}}{S_{ij}}\right)^2 \tag{2}$$

20 S_{ij} is the error (uncertainty) of each measurement data point. In an ideal case, the Q value of the model should approach the expected Q value (Q_{exp}) which is equal to the degree of freedom of the model solution. For mass spectra data, this is approximately equal to the size of the original data matrix, X:

$$Q_{exp} \approx n \cdot m \tag{3}$$

Different algorithms have been developed to solve the PMF model (e.g. Hoyer, 2004; Lu and Wu, 2004; Paatero, 1999).

25 In this study, we used the PMF2 algorithm with robust, least square optimisation, which is included in the PMF Evaluation Tool (Ulbrich et al., 2009) for Igor Pro 7 (WaveMetrics, Inc., Portland, Oregon). We calculated solutions with 1 to 12 factors. For each solution, 5 rotations (fpeak -1.0 to +1.0) were calculated, and for each original solution (fpeak=0) 6 different seed values were tested.

As an additional measure for the goodness of fit, we calculate the fraction of explained absolute variance ($Ratio_{exp}$):

$$absVar_{total} = \sum_{ij} |\boldsymbol{X}_{ij} - \overline{X}_\iota| \tag{4}$$

$$absVar_{explained} = \sum_{ij} |\boldsymbol{R}_{ij} - \overline{X}_\iota| \tag{5}$$

$$Ratio_{exp} = \frac{absVar_{explained}}{absVar_{total}} \tag{6}$$

where $\boldsymbol{R}_{ij}$ is the value in the reconstructed data matrix ($\boldsymbol{R} = \boldsymbol{GF}$) for each ion i and observation j, $\overline{X}_\iota$ is the average measured value of the ion i, $absVar_{total}$ and $absVar_{explained}$ are the total and explained absolute variance. Note that we use the absolute distance between the average values and the measured/reconstructed data instead of the square of this distance.

PMF has been widely used for analysing time series of mass spectra data in the atmospheric science community. However, the model does not utilise the information of the time axis in the optimisation process. Rather, it is a method that can be used to analyse a set of mass spectra which were obtained at different time points during the desorption cycle of FIGAERO and for different particle sampling conditions. This means that PMF will create the same model output if the x values in the dataset are a real time series (Figure 2b), a temperature ramp (Figure 2c) or simply an index with numbers (Figure 2a). Thus, data from separate thermogram scans with FIGAERO-CIMS can be combined to larger datasets and analysed together with PMF. Analysing multiple thermogram scans together has the advantage that more data points are utilised to identify the factors (here, 90 mass spectra for each thermogram) and that factors can be compared directly between scans. Only when evaluating the model output, the real time series/temperature ramp is of interest to interpret the identified factors and compare their desorption temperature profiles between thermogram scans. In the graphic presentation of these combined "time series" (e.g. Figure 4), a data index was used as x values which is the desorption temperature of each thermogram plus an offset (200 per thermogram). This choice of x values preserves the shape of the thermogram in desorption temperature space. The individual thermograms are marked with roman numbers and the sampling conditions are given in the figure captions. For easier comparison of the shape of the desorption behaviour of the factors, they are plotted individually for each SOA type (e.g. Figure 5).

When performing PMF with the combined dataset with all available thermogram scans, the large number of factors (13 or more) necessary to explain the observed variability complicated the analysis and interpretation (see case study in SI section 1.4). Thus, the thermogram scans were grouped by SOA type (i.e., t_{evap} = 0.25 h & 4 h particles, dry & wet conditions of one SOA type: four thermogram scans per group). This pre-grouping reduced the number of factors in each group enhancing their interpretability while still enabling a direct investigation of the changes due to the

evaporation/humidification for one SOA type. But generally, splitting the data by SOA type or even knowing about such different SOA types/sources in the data is not a requirement for analysing a thermogram dataset with PMF.

2.3.2 Error schemes for PMF

To perform the PMF analysis, a data error S_{ij} must be defined. As visible from Eq. (2), the S_{ij} values have a strong influence on the outcome of the PMF model. The measurement error can be understood as a weighting mechanism giving more weight to data points with less uncertainty (Paatero and Hopke, 2003). Ideally, S_{ij} is the true measurement error of the dataset. For gas phase CIMS data, Yan et al. (2016) have suggested to calculate the measurement error assuming a Poisson type distribution of the counting error:

$$S_{ij} = a \cdot \sqrt{\frac{X_{ij}}{t_s}} + \sigma_{noise,i} \tag{7}$$

with X_{ij} signal intensity of the ion i, t_s sampling (averaging) interval in s, and $\sigma_{noise,i}$ the electronic noise for ion i. We applied a procedure equivalent to the one introduced by Yan et al. (2016) to derive the parameter a from analysing the distribution of signal noise. The detailed calculation for this type of error is given in the SI material. The resulting error values (Poisson-like, "PLerror") will trace the shape of the thermogram signal with higher absolute values for those parts of the thermogram with higher intensity (i.e., the "peak") giving less weight to this region (Figure S 1). This is the correct approach for the analysis of long time series data where rapid changes are most likely caused by instrument noise or data outliers.

For FIGAERO-CIMS thermograms, the main information lies in the rapidly increasing and decreasing part of the data (the "peak", data points 10 – 50 in Figure 2a) when compounds are desorbing from the FIGAERO filter and not in the slowly changing (or constant) part at high desorption temperatures (the "tail" points 50 – 90 in Figure 2a). During this analysis it was found that the thermal desorption peaks could not be modelled well with error values calculated using Eq 7 (see section 2.3.3 and Appendix A). Thus, a new error scheme that allowed for increased weighting of the thermal desorption peaks was also tested. In this scheme, a constant error value corresponding to the noise in the data at the end of the thermogram scan, is used for each thermogram scan (constant noise, "CNerror") such that:

$$S_{ij} = \sigma_{noise,i} \tag{8}$$

$\sigma_{noise,i}$ of each ion i is calculated in the same way as for the PLerror (see SI material for details). Note that by omitting the first term in Eq. 7, Eq. 8 does not correspond to the true measurement error of the FIGAERO-CIMS data. Rather, it is the simplest way of weighting the PMF runs to put more emphasis on each thermogram peak and less on the fronts and tails FigureS 1 shows an example of the values for the two error schemes for one exemplary ion. The signal to noise values

are up to 3 orders of magnitude higher in the peak region for the CNerror case clearly giving them a stronger weight in the optimisation. As a direct consequence of the modified error value, the value for Q/Q_{exp} is not expected to approach 1, but instead will reach a larger (used error values smaller than real measurement error) or smaller (used error values larger than real measurement error) value. Thus, most solutions from PMF with PLerror will have (much) lower Q and Q/Q_{exp}

5   values than any solution from PMF with CNerror. This also means that comparing the absolute Q or Q/Q_{exp} values between results from the different error schemes is not meaningful as a higher absolute error value will result in a lower Q value.

2.3.3   Selection of error scheme and number of factors ("best" solution)

Before the "best" solution from PMF can be identified by investigating the factor profiles and spectra, the impact of the two different error schemes on the PMF output needs to be determined by running PMF for all combined datasets with

10   both error schemes and comparing the output. As the comparison of the Q/Q_{exp} values between the error schemes is not meaningful, as pointed out above, the fraction of explained variance ($Ratio_{exp}$) and the reconstruction of the characteristic shape of the thermograms (i.e., time series of residuals) were the decisive criteria. In addition to the single Q/Q_{exp} value summed over all ions and observations (i.e., mass spectra) in each dataset, we calculated the time series of the Q contributions (Q_j) summed over all ions for each observation (mass spectrum), j, to identify which periods in the dataset

15   were not captured well by the investigated PMF solution.

$$Q_j = \sum_{i=1}^{n} \left(\frac{E_{ij}}{S_{ij}}\right)^2 \tag{9}$$

Similarly, we calculate Q_i as the sum over all observations (mass spectra), j, to investigate which ion has the strongest contribution to the overall Q value:

$$Q_i = \sum_{j=1}^{m} \left(\frac{E_{ij}}{S_{ij}}\right)^2 \tag{10}$$

20   For a given number of factors, the CNerror scheme results in higher $Ratio_{exp}$ values than the PLerror (Figure 3), i.e., a larger fraction of the observed variance is captured by the model. With the PLerror the maximum $Ratio_{exp}$ is 0.9 even with up to 12 factors while with the CNerror the values for $Ratio_{exp}$ are >0.95 already with 7 factors.

To highlight the difference in behaviour of the two error schemes we display the time series of the residual and Q_j values in Figure 4 for the highOC case for three solutions (6, 7, and 10 factors). With the PLerror, the residuals are much larger

25   than in the CNerror case (panels b and d). But due to the larger values of S_{ij} in the PLerror case, the Q/Q_{exp} values (panels c and e) are much smaller. Thus, the optimisation algorithm sees no need to further improve the model in the PLerror case. Contrarily, the smaller unscaled residual in the 6-factor solution with the CNerror leads to much higher Q/Q_{exp}

values, especially in the peak of thermograms III and IV. Here, the addition of one factor (from 6 to 7) improves both the residual and the Q_f/Q_{exp} values, and the new factor captures a characteristic behaviour we discuss below in section 3.3. This analysis together with the more detailed case study in Appendix A leads us to the conclusion that for this study and dataset the CNerror reconstructed the measured data best and yielded the most interpretable results. Thus, from here on

5 we only present results from PMF runs with the CNerror scheme.

The advantage of PMF, that no a priori information about $\boldsymbol{F}$, $\boldsymbol{G}$, and p is needed for the analysis, is also a disadvantage. There is no absolute criterion for which number of factors (p) is correct or "best", but the chosen value strongly impacts the interpretation of the factors and their profiles. In the ideal case, when the true measurement errors are used, Q/Q_{exp} approaches 1 and a solution with Q/Q_{exp} close enough to 1 may be considered as the "best" or correct. But as we explained

10 in the previous paragraph, PMF performed much better for FIGAERO-CIMS data if the "unrealistic" CNerror scheme was used, and thus Q/Q_{exp} are not necessarily meaningful. However, the shape of the Q/Q_{exp} vs number of factors curve can be used to judge the impact of introducing another factor, i.e., a large change in Q/Q_{exp} suggests the new factor explains a large fraction of the variability in the data (Ulbrich et al., 2009). We investigated this for the PMF runs for each SOA type (Figure 3 and Figure S 2). The largest changes in Q/Q_{exp} are achieved already by increasing from 2 to 3 factors.

15 Further factor addition leads to a steady decrease of Q/Q_{exp}. In this case, the $Ratio_{exp}$ values are more helpful. Strong increases of $Ratio_{exp}$ are observed for increasing the number of factors to 6 (medium- and highOC case) or 8 (lowOC case).

As shown by Yan et al. (2016) for gas phase CIMS data, a solution with a low overall Q/Q_{exp} value may still have large variations in the scaled residual with time or with different ions. We carefully investigated especially the time series

20 (Q_j/Q_{exp}) of individual ions (e.g. $C_5H_5O_6^-$ in Figure A 1b and c) and present details of this case study in Appendix A. For each SOA type, there were a few specific ions which were not captured well in the dataset until a certain number of factors was chosen (e.g. 7 in the highOC case) even if the overall fraction of explained variance for the solutions was already larger than 95% and changed very little with further factor addition. We decided to choose the PMF solution with the smallest number of factors which still described the characteristic behaviour of most ion thermograms. These were the

25 solutions with 9, 7, and 7 factors for the low-, medium-, and highOC cases, respectively.

3   Results and Discussion

3.1   PMF factor interpretation

The three evaporation datasets (one for each SOA type) were analysed with PMF using the CNerror scheme and the results for the chosen "best" solutions are shown in Figure 5, Figure 6, and Figure 7 (and with "stacked" factor contribution

30 in Figure S 4, Figure S 5, and Figure S 6). In the following paragraphs, the first letter in the labels of factors indicates if

they are from the low- (L), medium- (M) or highOC (H) case, and the second letter identifies the factor type (V, B, D, and C; see below).

Generally, there were three main types of thermogram profiles for all factors: volatility class (type V) with a single, distinct peak (LV1 – 5, MV1 – 5, and HV1 – 5), type background (type B) with mostly constant contribution over the full T_{desorp} range (LB1, MB1, and HB1), and decomposition (type D) with mostly very broad peaks at $T_{desorp} < 65$ °C and an increase at $T_{desorp} > 110$ °C (LD1, MD1, and HD1).

Factors of type V do not contribute to the filter blank thermograms (Figure S 3) indicating that these factors are linked to compounds only present in the sampled aerosol particles. With the exception of the highOC wet case (which we discuss in detail in section 3.3), the peak position (T_{max}) of type V factors changes very little with aerosol age or water content (Table 2). Only the contribution of these factors to the total signal changes with isothermal evaporation or humidification. For each V-type factor, we could identify ions with thermogram shapes similar to the thermogram profile of the individual factors. This means that especially the V-type factors at high desorption temperature are not simply a better mathematical description of the tails of some ion thermograms, but represent real compounds desorbing from the FIGAERO filter at high desorption temperatures. Thus, we interpret the type V factors as volatility classes. Compounds with the same thermal desorption behaviour (i.e., volatility) are grouped into one type V factor which is characterised by its T_{max} value. Note that for the three different SOA types the starting particle composition was significantly different. So even if the T_{max} values for two factors of different SOA type, e.g., LV2, MV2, and HV1(dry cases), differ only by ~5 °C, the compounds contributing to them are not the same, i.e., the factor mass spectra for LV2, MV2, and HV1 are significantly different. We elaborate on the reasons for these differences in SI section 1.3 and 1.4.

Type B factors show contributions to the signal of sample thermograms and filter blanks (Figure S 3). For LB1, MB1, and HB1, the very shallow thermogram profile and the similar absolute signal strength despite different mass loadings on the FIGAERO filter indicate that these are instrument background factors. For some samples, especially those with high overall filter loading, the thermogram profile of the type B factors show a decrease to almost 0 for T_{desorp} ~60 – ~120 °C. This may indicate that part of the background signal in this temperature range is assigned into other factors ("factor blending/mixing"). But as the overall background in these few cases is $200 – 400$ ct s^{-1} while the signals of the V-type factors are more than 10 times higher, this factor blending will have a minor effect on the shape and T_{max} values of the V-type factors and thus the interpretation of the PMF solution. For the parts of the thermograms with lower signal strength and samples with low overall mass loading on the filter, the signal of the B-type factors stays constant at a value comparable to that observed for the filter blank samples. For all SOA types, the mass spectra of these factors are dominated by single ions typically associated with FIGAERO-CIMS background (e.g. fluorine containing compounds, formic acid, and lactic acid). According to the uncentered correlation method (contrast angle/ dot product) MB1 and HB1 are

reasonably similar. For the lowOC case, some of the instrument background is apparently assigned to the contamination factors (LC1&2, see below), thus decreasing the degree of similarity between LB1 and the other B factors.

Type D factors are the most difficult to interpret as they have contribution to the signal for both filter blank and sample thermograms, but the contribution can vary with the collected mass loading on the filter for sample thermograms. The

5   factor mass spectra (LD1, MD1, and HD1) show mostly contribution from ions with $M_w < 200$ Da, but the thermogram profiles exhibit a strong increase at $T_{desorp} > 110$ °C especially in filter blank thermograms. This suggests that the detected low M_w compounds in these factors are thermal decomposition products of larger, low volatile, but thermally unstable compounds. But in some cases (e.g. mediumOC dry, $t_{evap} = 0.25$ h and 4 h, Figure 6a and b) there is a second peak at much lower T_{desorp} (< 65 °C) which is in the range where compounds of the detected composition are expected to desorb.

10 This suggests that the ions grouped into the type D factors can stem from two "sources" – direct desorption ($T_{desorp} < \sim100$ °C) and thermal decomposition ($T_{desorp} > \sim100$ °C) – and PMF is not able to separate them as either their composition or their desorption behaviour is too similar. Consequently, type D factors have to be analysed carefully and interpreted as desorption at low T_{desorp} and decomposition at high T_{desorp}. Also, the instrument background contribution needs to be estimated from the filter blank thermograms. For the lowOC case, LD1 is dominated by compounds coming

15 from the filter/instrument background as the factor thermogram profile does not change with the collected sample mass and there is still contribution of the factor below $T_{desorp} < 100$ °C after 4 h of isothermal evaporation (Figure S 3a). For mediumOC, the direct desorption part ($T_{desorp} < 100$ °C) of MD1 is removed with isothermal evaporation which suggests that at least this part of the factor stems from the collected sample and not just the instrument/filter background. The highOC case is discussed below in section 3.3.

20 For the lowOC dry, $t_{evap} = 0.25$ h sample, two additional factors (type C) were found. The factor mass spectra of LC1&2 are dominated by extremely high signals for formic and lactic acid, which are typically strong indications of a contamination on the FIGAERO filter due to handling. We could not determine in retrospect what happened to this specific sample collection to cause this obvious contamination, but between this and the next sample collection the FIGAERO filter was replaced, and several heating cycles were performed ensuring that no other sample was affected.

25 However, since PMF has identified the ions affected by this contamination and grouped them into LC1&2, these two factors can be omitted from further analysis removing the bias caused by this contamination.

Note that almost the same factors are produced by PMF independent of whether the filter blank measurements are added to the datasets or not. This shows that PMF can be a very helpful tool for data interpretation when no reliable instrument background measurements are available, or if the background varies strongly between samples. Then the identification of

30 B, D, and C type factors has to rely only on the thermogram profiles and factor mass spectra.

3.2 Composition changes due to evaporation

One set of type V factors (i.e., volatility classes) was identified and separated from instrument background contributions for each dataset consisting of one SOA type sampled after different time intervals of isothermal evaporation under dry and wet conditions. The contribution of a single factor to the total signal is calculated as the ratio of the integral of the thermogram profile of this factor to the total signal. The relative contribution of factors V1 – V5 for each sampling condition is shown in Figure 8 plotted vs the volume fraction remaining (VFR) measured in separate isothermal evaporation measurements (VFR values from Buchholz et al. (2019)). The corresponding figure with absolute signal contributions is shown in the SI material (Figure S 7). Note that always the residual particles after isothermal evaporation or humidification were collected on the FIGAERO filter. This means with decreasing VFR a larger fraction of the particle mass had evaporated prior to the FIGAERO-CIMS measurements. In the low- and mediumOC case (Figure 8a and b), the relative contributions of MV1&2 and LV1&2 (T_{max} in SVOC range) decreased with decreasing VFR while those of LV3-5 and MV3-5 (T_{max} in LVOC and ELVOC range) increased. During 4 h of dry isothermal evaporation a similar volume fraction was removed as in 0.25 h of isothermal evaporation under wet conditions. The very similar relative contribution of the V-type factors in these two samples suggests that the observed changes in chemical composition in the particles are indeed connected to the change in VFR (i.e., how much of the volatile material was removed before sampling) and not directly driven by other water induced processes. For these SOA types, the main process during physical aging in the RTC (i.e., long residence time in clean air) under dry and wet conditions was isothermal particle evaporation. Here, the particulate water mostly decreased the viscosity in the particles, thus decreasing kinetic transport limitations in the particle phase and increasing evaporation. This observation is in agreement with previous interpretation of this and comparable datasets (Buchholz et al., 2019; Yli-Juuti et al., 2017). The highOC case (Figure 8c) will be discussed in section 3.3.

From the factor contribution, the detailed changes in particle composition due to isothermal evaporation can be derived by analysing the trends in the factor mass spectra. With increasing T_{max} of the factors (i.e., decreasing volatility) the average M_w as well as the C chain length and number of O continuously increased from V1 to V5 (Table 1). The contribution of compounds with C>10 also increased, which suggests an increasing contribution of dimers/oligomers. This may explain why no clear trend in the O:C (or OS_c) values could be observed for the V-type factors. While the lower volatility compounds indeed contained more oxygen the simultaneous increase of the carbon chain length seems to compensate this, resulting in no obvious systematic increase in O:C ratios. Thus, we observe a correlation of volatility with average M_w but not with average O:C ratio of the factors.

As the more volatile factors (LV1&2 and MV1&2) were systematically removed with isothermal evaporation, the composition of the residual particles was more and more dominated by the less volatile factors (LV3-5 and MV3-5), i.e.,

by larger, higher M_w compounds, many of them dimers/oligomers. However, the V4&5 factors still had a significant contribution of low M_w compounds as well (Figure 5 and Figure 6). The ion and factor thermograms of $[C_8H_{12}O_5 + I]^-$ are shown as an example for such a relatively small, low M_w ion in Figure 9a and b. This ion had contributions to all 5 factors. In principle, it is possible that there are several isomers of this composition with significantly different volatility being grouped into V1-5 spreading ~4 orders of magnitude in C^*. But it seems more likely that the compounds of this composition contributing to V4&5 were products of thermal decomposition. If this was indeed the case, it means that there were compounds in the particles which have a volatility corresponding to even higher T_{max} than that of factors V4&5, but because they decompose at desorption temperatures >100 °C they are grouped into these factors/volatility classes. This is an indication that FIGAERO-CIMS data overestimates the volatility as already previously suggested (Lopez-Hilfiker et al., 2015; Schobesberger et al., 2018; Stark et al., 2017), and care has to be taken when using these volatility values for modelling purposes.

3.3 Composition changes due to aqueous phase chemistry

Similar to the low- and mediumOC case, highOC SOA particles showed enhanced evaporation under wet conditions (Buchholz et al., 2019). But in addition, strong signs for aqueous phase chemistry in the wet highOC case were already visible by comparing the mass spectra integrated over the whole thermogram scan. Several very small compounds ($M_w <$ 200 Da and C_4-C_7) increased their contribution under wet conditions. Also, the thermograms of these ions showed distinct shifts to higher T_{max} values in the wet cases (by up to 20 °C) and even the formation of new low volatility material under wet conditions. As discussed by Buchholz et al. (2019), the different behaviour of the highOC SOA is most likely due to higher fractions of (hydro-)peroxides in the particles caused by the much higher HO_2 concentrations in the OFR at the highOC oxidation conditions. Most peroxides are sensitive to hydrolysis which will initiate a range of reactions in the aqueous phase. The low volatility products of these reactions thermally decompose to similar fragments as did the peroxide precursor. Thus, the same groups of ions are detected but at a higher T_{desorp}.

In the PMF analysis results, the different behaviour in the highOC case is also directly visible comparing the dry, $t_{evap} = 0.25$ h and wet, $t_{evap} = 0.25$ h cases (Figure 7a and c). The contribution of the (semi-)volatile factor (HV1) was reduced, but the factor thermogram profile and T_{max} also changed. HV2&4 shift to higher T_{max} values and a new factor HV3 was introduced which contained mostly low M_w compounds. The least volatile factor, HV5, which contains mostly high M_w compounds, showed much less contribution. It is also noteworthy that HD1 showed a strong increase in the wet case, not just in relative contribution but also in absolute strength. Also, the shape of the factor thermogram profile (strong increase at $T_{desorp} > 100$ °C) indicates that in this case HD1 was dominated by thermal decomposition products. With

further isothermal evaporation under wet conditions, HV3 increased its contribution while HV1&2 were almost completely removed (Figure 7 and Figure 8). Note that HV3 also exhibited an increase in absolute contribution to the signal, i.e., compounds contributing to this factor were being produced (Figure S 7c).

The removal of HV1 can still be explained by particulate water acting as a plasticiser enhancing the isothermal evaporation comparable to the low- and mediumOC cases. But HV2 has a T_{max} value already in the LVOC range like LV3 or MV3, which do not show a similar decrease with isothermal evaporation under wet conditions. Thus, the observed changes can only be explained by chemical processes induced by the presence of water in the particles. These processes consume compounds which were mostly grouped into factors HV2 and HV5. The T_{max} shift of HV1 and HV4 indicates that some compounds grouped into these factors might have been affected as well. The reaction products are mostly detected as low M_W compounds in HV3 and HD1. While the compounds grouped into HV3 might still be desorbing as such from the filter, this seems extremely unlikely for the compounds in HD1 as it only starts to appear at desorption temperatures > 100 °C. Thus, many of the formed low volatility compounds must be thermally unstable.

In our previous work (Buchholz et al., 2019), we used the unexpectedly large shift of T_{max} of specific ions together with the formation of low volatile material at wet conditions as evidence for aqueous phase chemistry in the highOC case. With the results from PMF we can now show how this T_{max} shift in the highOC case is indeed different from those smaller ones observed for the other SOA types. The single ion thermograms for $[C_8H_{12}O_5+I]^-$ (strong ion in low- and mediumOC samples) and for $C_4H_3O_6^-$ (strong ion in highOC identified to be affected by aqueous chemistry) are shown in Figure 9. In the low- and mediumOC cases (Figure 9a and b), T_{max} changed by ~10 °C between the sample with least (dry, $t_{evap} = 0.25$ h) and with most isothermal evaporation (wet, $t_{evap} = 4$ h). This shift is solely caused by the removal of LV1&MV1 and partly LV2&MV2, i.e., by the isothermal evaporation of the volatile fraction at this composition. In the highOC case (Figure 9c), HV1 is also removed with isothermal evaporation, but the new factor HV3 dominates under wet conditions. The change in T_{max} by 40 °C between the dry, $t_{evap} = 0.25$ h case when HV1 dominates and the wet, $t_{evap} = 4$ h case when HV3 is the only contribution is then simply the difference in volatility between the original compounds detected with this composition and the ones formed by aqueous phase chemistry.

In the dry case, there is a small contribution of HV3 around 100 °C. This is most likely due to the described aqueous phase processes happening already inside the OFR which was operated at ~40% RH. The drying during size selection stopped these processes leading to very minor contribution of the reaction products to the particle phase. If the particle stayed at wet conditions, the reactions continued and created the compounds grouped into HV3. But apart from this, there has to be another source for the compounds in HV3 in the dry case as there is a small peak at 63 °C. However, this peak is a very minor contribution to the overall signal in the dry case while HV3 at 100 °C dominates the thermograms in the wet case.

The 7-factor solution presented here clearly identifies the main features in the thermal desorption data that are caused by aqueous phase processes in the highOC case. But this solution still has "mixed" factors containing some compounds that are affected by chemical processes and others that are not, leading to changes in T_{max} as described above. Increasing the number of factors in the solution to 10 (results not shown) splits up HB1 into 3 B-/D-type factors as well as HV5 into HV5'a which contributed mostly to the dry cases and HV5'b which only occurred in the wet cases. This shows that with more factors a better separation of the compounds affected by aqueous phase processes may be achieved, but many more factors than 10 may be needed and strong factor splitting (i.e. artificial separation) may occur.

4   Conclusions

To our knowledge, this is the first study applying a PMF analysis to high resolution FIGAERO-CIMS thermal desorption data and interpreting the PMF factors as volatility classes characterised by their T_{max} values. Although we used a very specific dataset from a focussed laboratory study, the introduced method can be applied to other FIGAERO-CIMS datasets. The nature of PMF allows to combine multiple separate FIGAERO-CIMS thermograms and investigate them together.

We found that it is very important to study the impact of the chosen "measurement error" on the PMF solutions before interpreting the results of the PMF analysis. Instead of the most realistic measurement error, an error scheme best suited to focus on the part of the data relevant to the research question should be chosen. In our case, the most interpretable results were achieved by applying a CNerror based on the noise of each ion.

PMF was able to separate the measured signal of each ion into instrument background, contamination, and collected aerosol mass. This separation worked even if no filter blank data was added to the datasets. However, adding filter blank measurements to the dataset simplified the identification of background factors. Identifying background factors in this way instead of simply subtracting periodically taken filter blank measurements is especially helpful, if an insufficient number of filter blank measurements were collected or if the background changed between filter blank samples. While for higher mass loading samples, there was some evidence that a small portion of the background signal was miss-assigned to other factors (factor mixing/blending), this did not occur for low concentration measurements where being able to determine the actual contribution of background compounds is more important. At low concentrations, the shape of the combined thermogram of the background may significantly alter the overall shape of the thermogram (e.g., shift the T_{max} value) and thus change the interpretation of the volatility of the collected aerosol.

The collected aerosol mass signal part was separated into (mostly) direct desorption factors (i.e., volatility classes) and thermal decomposition factors. Thermal decomposition became the dominant process for many low M_w ions observed at

temperatures above 120 °C. Then the observed "desorption" temperatures are actually the decomposition temperatures and thus give an upper limit for the true volatility of the parent compounds. This shows again that FIGAERO-CIMS measurements may overestimate the volatility of aerosol particles based on parameterisation of the overall composition but also on desorption temperatures as described by some previous studies (Lopez-Hilfiker et al., 2016; Schobesberger et al., 2018; Stark et al., 2017). The knowledge about the contribution of thermal decomposition to a thermogram measurement obtained with the PMF method presented here can be used e.g. to improve the input into process models. An example for such an application is presented in Tikkanen et al. (2019).

For each SOA type (i.e., α-pinene SOA of different oxidative age) 5 main volatility classes were identified in the chosen PMF solution. Isothermal evaporation prior to sampling with FIGAERO-CIMS systematically removed the more volatile factors with T_{max} values corresponding to SVOCs. Low M_w compounds remaining in the particles after evaporation were attributed to low volatility factors indicating that they most likely were products of thermal decomposition above ~100 °C. However, between ~100 and 120 °C thermal decomposition was still a minor process. In the highOC case, the aqueous phase chemistry occurring under wet conditions was captured by introducing a new factor and shifts in T_{max} for other factors. Both the educts and products (or thermal decomposition products of them) could be identified. This highlights how PMF analysis can help with identifying processes in the particle phase.

The highOC SOA in our study may not be representative of ambient SOA of the same OC ratio as it was formed under extremely strong oxidation conditions in an OFR. But the type of compounds affected by aqueous phase chemistry (i.e., organic compounds containing (hydro)peroxides or other functional groups which easily hydrolyse and then continue to react) are not unique to OFR reactors. One formation path of compounds containing several hydroperoxyl or peroxyacid groups is the auto-oxidation of terpenes in the gas-phase leading to highly oxygenated material (HOM) (Bianchi et al., 2019; Ehn et al., 2014). These compounds play an important role in particle growth and detected more and more in ambient measurements (Lee et al., 2018; Mohr et al., 2017). Another compound class which is possibly susceptible to hydrolysis is organo-nitrates (which did not occur in our study due to the experiment design). Thus, ambient aerosol will probably not show as clear signs of aqueous phase chemistry as our high OC case, but it is very likely that such processes occur to some degree and may be detected with the PMF analysis of FIGAERO thermogram data.We like to point out that picking the "best" solution of PMF may have subjective bias and that there is no guarantee that we selected the truly optimal solution. But even if a higher number of factors was chosen, the overall interpretation of the factors was the same as the additional factors were added in all thermograms in the dataset typically splitting one of the previously identified factors. The influence of the background and thermal decomposition was still separated from the V-type factor and within one set of V-type factors for one SOA type there was very little variation in T_{max} values. Different degrees of isothermal evaporation of the particles prior to FIGAERO sampling were still reconstructed by decreasing the contribution of the

most volatile factors. Only in the highOC case where chemical processes altered the particle composition enough, the factor interpretability may improve with increasing factor numbers as it is likely that at some point, the "wet chemistry" factors will be completely separated from the other factors, i.e., there will be multiple factor only occurring in the wet samples and the T_{max} values of the other factors will be constant. But as long as the chosen solution can capture the main features of the chemical process, mixed/blended factors are no hindrance for identifying the compounds affected by the chemical processes. Thus, even without a hard criterion to determine the "correct" number of factors, the PMF analysis of FIGAERO-CIMS data gives valuable insights into processes in the particle phase.

The example ions shown in Figure 9 highlight how important it is to allow a single ion to contribute to more than one class/factor when analysing FIGAERO-CIMS data. Clustering techniques, as for example described by Koss et al. (2019) or Li et al. (2019), which assign each detected ion/composition to a single cluster, are incapable of capturing such a behaviour, i.e., the shift of T_{max} between two measured thermograms due to the selective removal of some of the isomers/thermal decomposition products. For the investigated dataset, we artificially removed the volatile fraction at a set ion composition with the prior isothermal evaporation. However, as the composition of ambient aerosol changes with time, e.g. by changes in the gas-particle partitioning or due to aging processes, the ratio between different isomers or the educts for thermal decomposition will change causing similar features in single ion thermograms of FIGAERO-CIMS data.

The next step for this method (PMF analysis of thermal desorption data) is the application to ambient measurements. Typically, the thermal desorption data of each sample in such a time series of FIGAERO-CIMS measurements is integrated over the desorption cycle to create a time series of chemical composition which can be analysed with PMF to identify sources/OA types. By including the "extra dimension" of the thermal desorption in the analysis, this time series is changed to a sequence of thermograms. Real time series specific (i.e., source specific) grouping in PMF will then only occur for compounds which also have similar thermograms (i.e., similar volatility). A simplified demonstration of that is found in SI section 1.3. However, the additional volatility information will help with factor interpretation. Preliminary tests with a dataset of ambient FIGAERO-CIMS measurements show that PMF analysis of thermal desorption data creates factors that can be associated with ambient sources (i.e., which precursors and/or processes created the aerosol) and/or OA type (e.g. fresh and aged OA). In addition to this, the analysis provides detailed information on the volatility of each of these sources or OA types while also showing how much of the signal is affected by thermal decomposition. This information on the contribution of thermal decomposition is crucial when the FIGAERO-CIMS data is used to identify the detailed composition or volatility of SOA particles. It will be very interesting to compare the factors identified with PMF of thermal desorption data with the "traditional" PMF analysis of the mass spectra data integrated over each thermogram scan. Details of this investigation will be the content of a future publication.

Appendix A Case study on impact of different error schemes

As briefly described in sections 2.3.2 and 2.3.3, we investigated the impact of two different error schemes (CNerror and PLerror) on the results of PMF. The highOC dataset was selected for this case study as the ions affected by aqueous phase chemistry proved to be the most difficult to capture.

In the PLerror case, the residual time series for the total ion signal (Figure 4d) was positive at all times (i.e., the total reconstructed signal was lower than the measured data) and decreased very little when increasing the factor number from 6 to 10. While the residual time series of individual ions did exhibit negative values (Figure A 1d and Figure A 2d), their distribution was still biased towards positive values (i.e., overall under-predicting the measured data). In the CNerror case (Figure 4b), in particular, the residual time series is spread more symmetric around 0 and additionally exhibits much lower values than in the comparable PLerror case, particularly for thermograms III and IV (particles under wet conditions).

To illustrate why there is no further improvement in the PMF results with the PLerror scheme and to show at which part of the dataset the error schemes create different results, we investigate the behaviour of the PMF solutions for individual ions. We select two ions with similar signal strength. One characteristic for ions captured well with both error schemes ($[C_7H_8O_6 + I]^-$, Figure A 2) and one ($C_5H_5O_6^-$, Figure A 1) where the PLerror scheme does not perform well. Note that the later represents the group contained mostly ions which were affected by aqueous phase chemistry. For the 6-factor solution (red line in Figure A 1b and d), the residual time series for this ion have similar values for thermogram scans III and IV in both error schemes, but increasing the numbers of factors by 1 seems to have a noticeable effect only in the CNerror case. This is because here, the Q_{ion} values ($Q_{ion} = \left(\frac{E_{ion}}{S_{ion}}\right)^2$) are extremely high for that part of the dataset (red line panel c). Investigating the Q_i values summed over all observations (mass spectra) show that this ion ($C_5H_5O_6^-$) has the 5th highest contribution to overall Q/Q_{exp}. The other ions with such high single contribution to Q/Q_{exp} exhibit very similar behaviour of their residuals and Q_{ion} values. Together they account for 15% of the overall Q/Q_{exp} value in the 6-factor case. So, adding an additional factor describing that portion of the dataset will strongly decrease Q_{ion} and with it Q/Q_{exp} indicating a better fit. In the PLerror case, the Q_{ion} values exhibit very similar profiles for all four thermogram scans (Figure A1d and e). Thus, changing any parameter for $C_5H_5O_6^-$ will have little effect on the Q_{ion} values and therefore on overall Q/Q_{exp}. This example clearly shows how the selection of the error values guides the focus of PMF, i.e., which part of the dataset still needs improvement when the number of factors is increased. In Figure A 3, the contribution of each factor to the signal of $C_5H_5O_6^-$ is shown by coloured areas for the 6 (top) and 7 (bottom) factor solutions for CNerror (a and c) and PLerror (b and d) to highlight the change between 6 and 7 factors for this ion. In addition to reducing the

residual for the peaks in thermograms III and IV, using CNerror, the additional factor substantially alters the factor time series for this ion, therefore likely affecting our interpretation of these factors, presumably towards improved accuracy. Indeed the "new" factor F3 was identified in section 3.3 as HV3 containing the products of the chemical reactions in the aqueous phase.

5 This error scheme depending performance of PMF is not controlled by the signal strength of the ion or the ratio between signals of combined thermograms. The two example ions were chosen explicitly because of their similar signal strength in all thermograms (compare Figure A 1a and Figure A 2a). It rather seems that the PLerror does not assign enough weight to the peak region of the ion thermograms. Thus, it cannot resolve the changes in peak shape (i.e., the large shift towards higher desorption temperatures). As the shift is caused by specific processes in the particle phase, PMF with the PLerror
10 will not identify these processes.

These two observations, the CNerror explaining more of the observed variance in general and capturing the complex chemical processes in the particles, leads us to the conclusion that for this study and dataset the CNerror yields the more interpretable results and should be used. Even though it is not be the "true" measurement error of the data.

Appendix B Mathematical symbols

Table B1 Mathematical symbols and notations used in the equations throughout the paper.

symbol	explanation
X, X_{ij}	data matrix ($n \times m$) and data matrix element
p	number of factors
m	number of observations (mass spectra) in the dataset
n	number of ions in the dataset
G	factorization matrix containing the factor thermograms as columns ($n \times p$)
F	factorization matrix containing the factor mass spectra as rows ($p \times m$)
E, E_{ij}	residual matrix and residual matrix element
R, R_{ij}	reconstructed data matrix ($R = GF$) and reconstructed data matrix element
S, S_{ij}	measurement error matrix and error matrix element
$absVar_{total}$	total absolute variance
$absVar_{exp}$	explained absolute variance
$Ratio_{exp}$	Ratio of explained to total absolute variance
Q	square of the residual scaled with the error summed over all ions and observations (mass spectra)
Q_{exp}	expected Q value, in the ideal case with the "true" measurement error equal to $n \times m$
Q_j	square of the residual scaled with the error summed over all observations (mass spectra)
Q_i	square of the residual scaled with the error summed over all ions
Q_{ion}	square of the residual scaled with the error for a single ion as time series
Q/Q_{exp}	optimisation parameter in PMF

Data availability: The dataset used in this study is available upon request from the corresponding author.

Author contributions: AB, AY, and CM conducted the FIGAERO-CIMS measurements. The data was processed by AY, WH, and CM. AB conducted the PMF analysis. All authors participated in the interpretation of the data. AB wrote the manuscript with contributions from all co-authors.

Competing interests: The authors declare that they have no conflict of interest.

Acknowledgments: The authors would like to acknowledge the support during the collection of this dataset by Celia Faiola, Eetu Kari, Liqing Hao, and Sergey Nizkorodov. Furthermore, we want to thank Andrew Lambe for his help installing PAM.

Financial support: We thank the European Research Council (ERC StG QAPPA 335478), the Academy of Finland Centre of Excellence program (decision 307331) and the Academy of Finland (grants 299544, 317373, and 310682) for financial support.

5   References

Bannan, T. J., Le Breton, M., Priestley, M., Worrall, S. D., Bacak, A., Marsden, N. A., Mehra, A., Hammes, J., Hallquist, M., Alfarra, M. R., Krieger, U. K., Reid, J. P., Jayne, J., Robinson, W., McFiggans, G., Coe, H., Percival, C. J. and Topping, D.: A method for extracting calibrated volatility information from the FIGAERO-HR-ToF-CIMS and its experimental application, Atmos. Meas. Tech., 12(3), 1429–1439, doi:10.5194/amt-12-1429-2019, 2019.

Bianchi, F., Kurtén, T., Riva, M., Mohr, C., Rissanen, M. P., Roldin, P., Berndt, T., Crounse, J. D., Wennberg, P. O., Mentel, T. F., Wildt, J., Junninen, H., Jokinen, T., Kulmala, M., Worsnop, D. R., Thornton, J. A., Donahue, N., Kjaergaard, H. G. and Ehn, M.: Highly Oxygenated Organic Molecules (HOM) from Gas-Phase Autoxidation Involving Peroxy Radicals: A Key Contributor to Atmospheric Aerosol, Chem. Rev., 119(6), 3472–3509, doi:10.1021/acs.chemrev.8b00395, 2019.

Buchholz, A., Lambe, A. T., Ylisirniö, A., Li, Z., Tikkanen, O. P., Faiola, C., Kari, E., Hao, L., Luoma, O., Huang, W., Mohr, C., Worsnop, D. R., Nizkorodov, S. A., Yli-Juuti, T., Schobesberger, S. and Virtanen, A.: Insights into the O: C-dependent mechanisms controlling the evaporation of α-pinene secondary organic aerosol particles, Atmos. Chem. Phys., 19(6), 4061–4073, doi:10.5194/acp-19-4061-2019, 2019.

D'Ambro, E. L., Schobesberger, S., Zaveri, R. A., Shilling, J. E., Lee, B. H., Lopez-Hilfiker, F. D., Mohr, C. and Thornton, J. A.: Isothermal Evaporation of α-Pinene Ozonolysis SOA: Volatility, Phase State, and Oligomeric Composition, ACS Earth Sp. Chem., 2(10), 1058–1067, doi:10.1021/acsearthspacechem.8b00084, 2018.

D'Ambro, E. L., Schobesberger, S., Gaston, C. J., Lopez-Hilfiker, F. D., Lee, B. H., Liu, J., Zelenyuk, A., Bell, D., Cappa, C. D., Helgestad, T., Li, Z., Guenther, A., Wang, J., Wise, M., Caylor, R., Surratt, J. D., Riedel, T., Hyttinen, N., Salo, V.-T., Hasan, G., Kurtén, T., Shilling, J. E. and Thornton, J. A.: Chamber-based insights into the factors controlling IEPOX SOA yield, composition, and volatility, Atmos. Chem. Phys. Discuss., (August), 1–20, doi:10.5194/acp-2019-271, 2019.

Donahue, N. M., Robinson, A. L., Stanier, C. O. and Pandis, S. N.: Coupled partitioning, dilution, and chemical aging of semivolatile organics, Environ. Sci. Technol., 40(8), 2635–2643, doi:10.1021/es052297c, 2006.

Ehn, M., Thornton, J. A., Kleist, E., Sipilä, M., Junninen, H., Pullinen, I., Springer, M., Rubach, F., Tillmann, R., Lee, B., Lopez-Hilfiker, F., Andres, S., Acir, I. H., Rissanen, M., Jokinen, T., Schobesberger, S., Kangasluoma, J., Kontkanen, J., Nieminen, T., Kurtén, T., Nielsen, L. B., Jørgensen, S., Kjaergaard, H. G., Canagaratna, M., Maso, M. D., Berndt, T., Petäjä, T., Wahner, A., Kerminen, V. M., Kulmala, M., Worsnop, D. R., Wildt, J. and Mentel, T. F.: A large source of low-volatility secondary organic aerosol, Nature, 506(7489), 476–479, doi:10.1038/nature13032, 2014.

Glasius, M. and Goldstein, A. H.: Recent Discoveries and Future Challenges in Atmospheric Organic Chemistry, Environ. Sci. Technol., 50(6), 2754–2764, doi:10.1021/acs.est.5b05105, 2016.

Goldstein, A. H. and Galbally, I. E.: Known and Unexplored Organic Constituents in the Earth's Atmosphere, Environ. Sci. Technol., 41(5), 1514–1521, doi:10.1021/es072476p, 2007.

Herrmann, H.: Kinetics of Aqueous Phase Reactions Relevant for Atmospheric Chemistry, Chem. Rev., 103(12), 4691–4716, doi:10.1021/cr020658q, 2003.

Hoyer, P. O.: Non-negative matrix factorization with sparseness constraints, J. Mach. Learn. Res., 5, 1457–1469, 2004.

Jimenez, J. L., Canagaratna, M. R., Donahue, N. M., Prevot, A. S. H., Zhang, Q., Kroll, J. H., DeCarlo, P. F., Allan, J. D., Coe, H., Ng, N. L., Aiken, A. C., Docherty, K. S., Ulbrich, I. M., Grieshop, A. P., Robinson, A. L., Duplissy, J., Smith, J. D., Wilson, K. R., Lanz, V. A., Hueglin, C., Sun, Y. L., Tian, J., Laaksonen, A., Raatikainen, T., Rautiainen, J., Vaattovaara, P., Ehn, M., Kulmala, M., Tomlinson, J. M., Collins, D. R., Cubison, M. J., Dunlea, J., Huffman, J. A., Onasch, T. B., Alfarra, M. R., Williams, P. I., Bower, K., Kondo, Y., Schneider, J., Drewnick, F., Borrmann, S., Weimer, S., Demerjian, K., Salcedo, D., Cottrell, L., Griffin, R., Takami, A., Miyoshi, T., Hatakeyama, S., Shimono, A., Sun, J. Y., Zhang, Y. M., Dzepina, K., Kimmel, J. R., Sueper, D., Jayne, J. T., Herndon, S. C., Trimborn, A. M., Williams, L. R., Wood, E. C., Middlebrook, A. M., Kolb, C. E., Baltensperger, U. and Worsnop, D. R.: Evolution of Organic Aerosols in the Atmosphere, Science (80-.)., 326(5959), 1525–1529, doi:10.1126/science.1180353, 2009.

Junninen, H., Ehn, M., Petäjä, Luosujärvi, L., Kotiaho, T., Kostiainen, R., Rohner, U., Gonin, M., Fuhrer, K., Kulmala, M. and Worsnop, D. R.: A high-resolution mass spectrometer to measure atmospheric ion composition, Atmos. Meas. Tech., 3(4), 1039–1053, doi:10.5194/amt-3-1039-2010, 2010.

Koss, A. R., Canagaratna, M. R., Zaytsev, A., Krechmer, J. E., Breitenlechner, M., Nihill, K., Lim, C., Rowe, J. C., Roscioli, J. R., Keutsch, F. N. and Kroll, J. H.: Dimensionality-reduction techniques for complex mass spectrometric datasets: application to laboratory atmospheric organic oxidation experiments, Atmos. Chem. Phys. Discuss., (June), 1–42, doi:10.5194/acp-2019-469, 2019.

Kroll, J. H. and Seinfeld, J. H.: Chemistry of secondary organic aerosol: Formation and evolution of low-volatility organics in the atmosphere, Atmos. Environ., 42(16), 3593–3624, doi:10.1016/j.atmosenv.2008.01.003, 2008.

Lanz, V. A., Alfarra, M. R., Baltensperger, U., Buchmann, B., Hueglin, C. and Prévôt, A. S. H.: Source apportionment of submicron organic aerosols at an urban site by factor analytical modelling of aerosol mass spectra, Atmos. Chem. Phys., 7(6), 1503–1522, doi:10.5194/acp-7-1503-2007, 2007.

Lee, B. H., Lopez-Hilfiker, F. D., Mohr, C., Kurtén, T., Worsnop, D. R. and Thornton, J. A.: An iodide-adduct high-resolution time-of-flight chemical-ionization mass spectrometer: Application to atmospheric inorganic and organic compounds, Environ. Sci. Technol., 48(11), 6309–6317, doi:10.1021/es500362a, 2014.

Lee, B. H., Lopez-Hilfiker, F. D., D'Ambro, E. L., Zhou, P., Boy, M., Petäjä, T., Hao, L., Virtanen, A. and Thornton, J. A.: Semi-volatile and highly oxygenated gaseous and particulate organic compounds observed above a boreal forest canopy, Atmos. Chem. Phys., 18(15), 11547–11562, doi:10.5194/acp-18-11547-2018, 2018.

Li, Z., D'Ambro, E. L., Schobesberger, S., Gaston, C. J., Lopez-Hilfiker, F. D., Liu, J., Shilling, J. E., Thornton, J. A. and Cappa, C. D.: A robust clustering algorithm for analysis of composition-dependent organic aerosol thermal desorption measurements, Atmos. Chem. Phys. Discuss., (September), 1–52, doi:10.5194/acp-2019-733, 2019.

Liu, P., Li, Y. J., Wang, Y., Gilles, M. K., Zaveri, R. A., Bertram, A. K. and Martin, S. T.: Lability of secondary organic particulate matter, Proc. Natl. Acad. Sci. U. S. A., 113(45), 12643–12648, doi:10.1073/pnas.1603138113, 2016.

Lopez-Hilfiker, F. D., Mohr, C., Ehn, M., Rubach, F., Kleist, E., Wildt, J., Mentel, T. F., Lutz, A., Hallquist, M., Worsnop, D. and Thornton, J. A.: A novel method for online analysis of gas and particle composition: description and evaluation of a Filter Inlet for Gases and AEROsols (FIGAERO), Atmos. Meas. Tech., 7, 983–1001, doi:10.5194/amt-7-983-2014, 2014.

Lopez-Hilfiker, F. D., Mohr, C., Ehn, M., Rubach, F., Kleist, E., Wildt, J., Mentel, T. F., Carrasquillo, A. J., Daumit, K.

E., Hunter, J. F., Kroll, J. H., Worsnop, D. R. and Thornton, J. A.: Phase partitioning and volatility of secondary organic aerosol components formed from α-pinene ozonolysis and OH oxidation: The importance of accretion products and other low volatility compounds, Atmos. Chem. Phys., 15(14), 7765–7776, doi:10.5194/acp-15-7765-2015, 2015.

Lopez-Hilfiker, F. D., Mohr, C., D'Ambro, E. L., Lutz, A., Riedel, T. P., Gaston, C. J., Iyer, S., Zhang, Z., Gold, A.,
5 Surratt, J. D., Lee, B. H., Kurten, T., Hu, W. W., Jimenez, J., Hallquist, M. and Thornton, J. A.: Molecular Composition and Volatility of Organic Aerosol in the Southeastern U.S.: Implications for IEPOX Derived SOA, Environ. Sci. Technol., 50(5), 2200–2209, doi:10.1021/acs.est.5b04769, 2016.

Lu, J. and Wu, L.: Technical details and programming guide for a general two-way positive matrix factorization algorithm, J. Chemom., 18(12), 519–525, doi:10.1002/cem.894, 2004.

10 Mohr, C., Lopez-Hilfiker, F. D., Yli-Juuti, T., Heitto, A., Lutz, A., Hallquist, M., D'Ambro, E. L., Rissanen, M. P., Hao, L., Schobesberger, S., Kulmala, M., Mauldin, R. L., Makkonen, U., Sipilä, M., Petäjä, T. and Thornton, J. A.: Ambient observations of dimers from terpene oxidation in the gas phase: Implications for new particle formation and growth, Geophys. Res. Lett., 44(6), 2958–2966, doi:10.1002/2017GL072718, 2017.

Paatero, P.: The Multilinear Engine—A Table-Driven, Least Squares Program for Solving Multilinear Problems,
15 Including the n-Way Parallel Factor Analysis Model, J. Comput. Graph. Stat., 8(4), 854–888, doi:10.1080/10618600.1999.10474853, 1999.

Paatero, P. and Hopke, P. K.: Discarding or downweighting high-noise variables in factor analytic models, in Analytica Chimica Acta, vol. 490, pp. 277–289, Elsevier., 2003.

Paatero, P. and Tapper, U.: Positive matrix factorization: A non-negative factor model with optimal utilization of error
20 estimates of data values, Environmetrics, 5(2), 111–126, doi:10.1002/env.3170050203, 1994.

Pankow, J. F.: An absorption model of gas/particle partitioning of organic compounds in the atmosphere, Atmos. Environ., 28(2), 185–188, doi:10.1016/1352-2310(94)90093-0, 1994a.

Pankow, J. F.: An absorption model of the gas/aerosol partitioning involved in the formation of secondary organic aerosol, Atmos. Environ., 28(2), 189–193, doi:10.1016/1352-2310(94)90094-9, 1994b.

25 Pankow, J. F., Seinfeld, J. H., Asher, W. E. and Erdakos, G. B.: Modeling the formation of secondary organic aerosol. 1. Application of theoretical principles to measurements obtained in the α-pinene/, β-pinene/, sabinene/, Δ3-carene/, and cyclohexene/ozone systems, Environ. Sci. Technol., 35(6), 1164–1172, doi:10.1021/es001321d, 2001.

Renbaum-Wolff, L., Grayson, J. W., Bateman, A. P., Kuwata, M., Sellier, M., Murray, B. J., Shilling, J. E., Martin, S. T. and Bertram, A. K.: Viscosity of α-pinene secondary organic material and implications for particle growth and reactivity.,
30 Proc. Natl. Acad. Sci. U. S. A., 110(20), 8014–8019, doi:10.1073/pnas.1219548110, 2013.

Schobesberger, S., D'Ambro, E. L., Lopez-Hilfiker, F. D., Mohr, C. and Thornton, J. A.: A model framework to retrieve thermodynamic and kinetic properties of organic aerosol from composition-resolved thermal desorption measurements, Atmos. Chem. Phys., 18(20), 14757–14785, doi:10.5194/acp-18-14757-2018, 2018.

Stark, H., Yatavelli, R. L. N., Thompson, S. L., Kang, H., Krechmer, J. E., Kimmel, J. R., Palm, B. B., Hu, W., Hayes, P.
35 L., Day, D. A., Campuzano-Jost, P., Canagaratna, M. R., Jayne, J. T., Worsnop, D. R. and Jimenez, J. L.: Impact of Thermal Decomposition on Thermal Desorption Instruments: Advantage of Thermogram Analysis for Quantifying Volatility Distributions of Organic Species, Environ. Sci. Technol., 51(15), 8491–8500, doi:10.1021/acs.est.7b00160, 2017.

Surratt, J. D., Lewandowski, M., Offenberg, J. H., Jaoui, M., Kleindienst, T. E., Edney, E. O. and Seinfeld, J. H.: Effect
40 of acidity on secondary organic aerosol formation from isoprene, Environ. Sci. Technol., 41(15), 5363–5369,

doi:10.1021/es0704176, 2007.

Tikkanen, O., Buchholz, A., Ylisirniö, A., Schobesberger, S. and Virtanen, A.: Comparing SOA volatility distributions derived from isothermal SOA particle evaporation data and FIGAERO-CIMS measurements, Atmos. Chem. Phys. Discuss., (November), 1–34, doi:10.5194/acp-2019-927, 2019.

5   Tolocka, M. P., Jang, M., Ginter, J. M., Cox, F. J., Kamens, R. M. and Johnston, M. V.: Formation of Oligomers in Secondary Organic Aerosol, Environ. Sci. Technol., 38(5), 1428–1434, doi:10.1021/es035030r, 2004.

Ulbrich, I. M., Canagaratna, M. R., Zhang, Q., Worsnop, D. R. and Jimenez, J. L.: Interpretation of organic components from Positive Matrix Factorization of aerosol mass spectrometric data, Atmos. Chem. Phys., 9(9), 2891–2918, doi:10.5194/acp-9-2891-2009, 2009.

10 Virtanen, A., Joutsensaari, J., Koop, T., Kannosto, J., Yli-Pirilä, P., Leskinen, J., Mäkelä, J. M., Holopainen, J. K., Pöschl, U., Kulmala, M., Worsnop, D. R. and Laaksonen, A.: An amorphous solid state of biogenic secondary organic aerosol particles, Nature, 467(7317), 824–827, doi:10.1038/nature09455, 2010.

Wang, D. S. and Hildebrandt Ruiz, L.: Chlorine-initiated oxidation of alkanes under high-NO conditions: Insights into secondary organic aerosol composition and volatility using a FIGAERO-CIMS, Atmos. Chem. Phys., 18(21), 15535–
15 15553, doi:10.5194/acp-18-15535-2018, 2018.

Wilson, J., Imre, D., Beránek, J., Shrivastava, M. and Zelenyuk, A.: Evaporation kinetics of laboratory-generated secondary organic aerosols at elevated relative humidity, Environ. Sci. Technol., 49(1), 243–249, doi:10.1021/es505331d, 2015.

Yan, C., Nie, W., Äijälä, M., Rissanen, M. P., Canagaratna, M. R., Massoli, P., Junninen, H., Jokinen, T., Sarnela, N.,
20 Häme, S. A. K., Schobesberger, S., Canonaco, F., Yao, L., Prévôt, A. S. H., Petäjä, T., Kulmala, M., Sipilä, M., Worsnop, D. R. and Ehn, M.: Source characterization of highly oxidized multifunctional compounds in a boreal forest environment using positive matrix factorization, Atmos. Chem. Phys., 16(19), 12715–12731, doi:10.5194/acp-16-12715-2016, 2016.

Yli-Juuti, T., Pajunoja, A., Tikkanen, O. P., Buchholz, A., Faiola, C., Väisänen, O., Hao, L., Kari, E., Peräkylä, O., Garmash, O., Shiraiwa, M., Ehn, M., Lehtinen, K. and Virtanen, A.: Factors controlling the evaporation of secondary
25 organic aerosol from a-pinene ozonolysis, Geophys. Res. Lett., 44(5), 2562–2570, doi:10.1002/2016GL072364, 2017.

6 Tables

Table 1: Signal weighted average values of elemental composition, O:C, OSc, and contribution of C>10 compounds for all factors.

ID	composition	M_w / g mol^{-1}	O:C	OSc	C>10 / %
LV1	$C_{8.6}H_{13.3}O_{5.2}$	213.4	0.66	-0.27	9.3
LV2	$C_{9.0}H_{14.2}O_{5.6}$	200.3	0.64	-0.30	12.7
LV3	$C_{10.3}H_{16.7}O_{6.8}$	249.7	0.70	-0.21	36.5
LV4	$C_{12.6}H_{21.8}O_{7.9}$	300.5	0.66	-0.39	65.2
LV5	$C_{12.5}H_{21.3}O_{8.5}$	308.2	0.72	-0.24	65.1
LD1	$C_{9.8}H_{15.4}O_{6.3}$	235.7	0.74	-0.05	33.8
LB1	$C_{9.7}H_{15.5}O_{6.2}$	234.8	0.78	0.00	38.3
LC1	$C_{8.6}H_{14.3}O_{5.2}$	201.9	0.81	-0.05	28.2
LC2	$C_{6.2}H_{9.5}O_{3.9}$	148.0	0.93	0.21	7.6
MV1	$C_{7.8}H_{11.6}O_{5.0}$	185.8	0.70	-0.12	7.6
MV2	$C_{8.1}H_{11.6}O_{5.8}$	202.3	0.76	0.07	4.1
MV3	$C_{9.0}H_{13.4}O_{6.5}$	226.6	0.76	0.01	15.4
MV4	$C_{10.1}H_{16.0}O_{7.4}$	257.1	0.80	0.02	38.3
MV5	$C_{11.3}H_{18.7}O_{7.6}$	276.5	0.73	-0.17	51.4
MD1	$C_{8.8}H_{13.5}O_{5.9}$	214.8	0.75	-0.01	7.6
MB1	$C_{9.8}H_{15.6}O_{6.1}$	235.5	0.79	0.02	38.9
HV1	$C_{7.0}H_{9.5}O_{5.6}$	184.7	0.90	0.43	6.2
HV2	$C_{7.9}H_{11.1}O_{6.3}$	208.6	0.86	0.29	8.5
HV3	$C_{7.7}H_{10.6}O_{6.3}$	204.3	0.92	0.44	12.9
HV4	$C_{8.4}H_{12.4}O_{6.6}$	219.4	0.87	0.23	18.6
HV5	$C_{10.0}H_{16.2}O_{6.8}$	247.4	0.76	-0.09	39.8
HD1	$C_{8.3}H_{12.3}O_{5.9}$	207.1	0.82	0.18	19.7
HB1	$C_{9.7}H_{15.5}O_{6.1}$	232.8	0.77	-0.02	38.4

Table 2: T_{max} values for all V-type factors. "-" indicates that there was not enough signal to determine T_{max} values.

ID	dry, t_{evap}=0.25h	dry, t_{evap}=4h	80%, t_{evap}=0.25h	80%, t_{evap}=4h
LV1	37.4	42.5	44.7	-
LV2	51.7	56.5	56.0	56.8
LV3	66.5	70.3	71.2	69.2
LV4	82.0	83.6	86.5	86.6
LV5	95.8	97.6	99.3	102.7
MV1	42.9	44.1	48.1	-
MV2	59.7	58.2	63.7	63.2
MV3	74.9	73.5	78.7	79.6
MV4	93.6	91.6	97.3	101.1
MV5	118.8	116.5	122.5	129.9
HV1	60.7	61.0	75.3	-
HV2	77.2	76.7	93.7	136.5
HV3	58.1	60.0	87.8	104.3
HV4	95.8	94.7	109.0	128.5
HV5	121.6	120.3	136.5	148.0

7   Figures
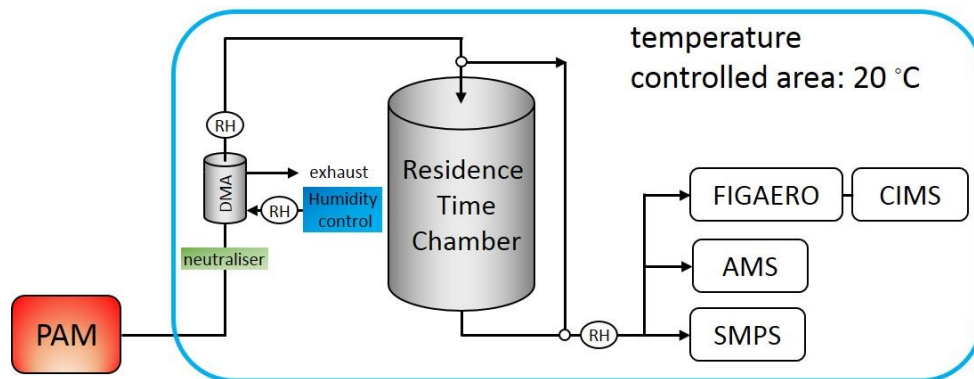
Figure 1: Schematic of experimental setup.
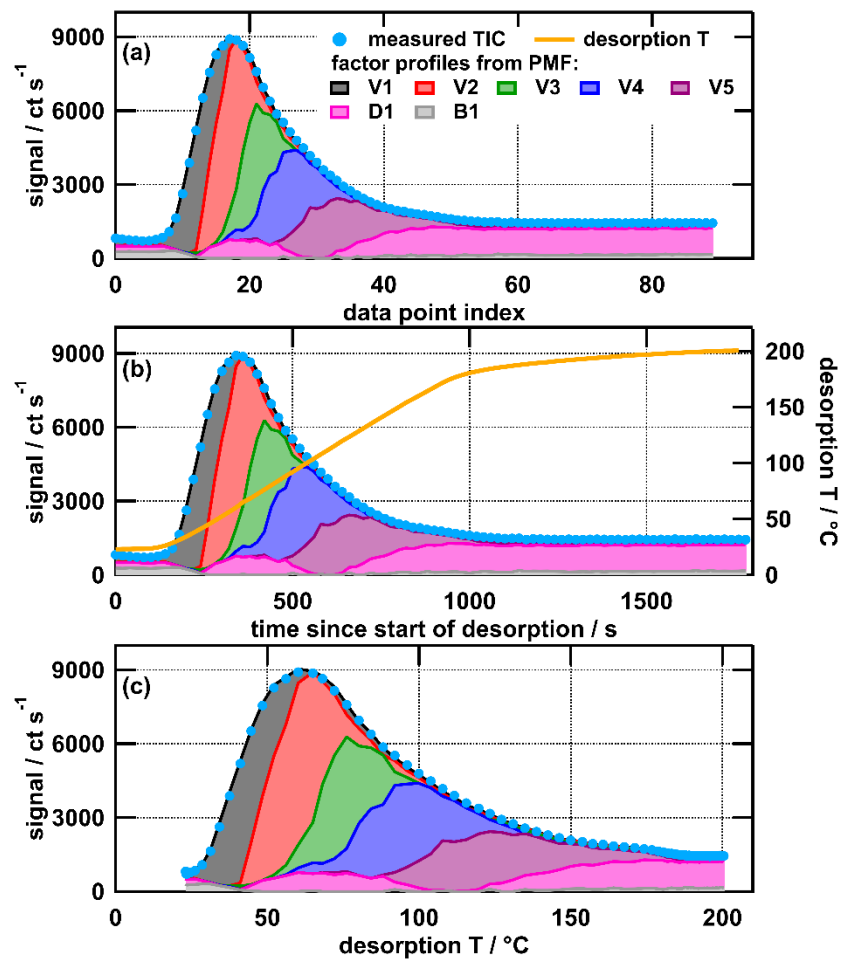
Figure 2: Measured total ion thermogram colour coded with the contribution of PMF model output factors for the mediumOC, $t_{evap} = 4$ h, wet case plotted vs data point index (a), time since start of desorption (b), and desorption temperature (c). Note that the desorption temperature ramp (b) is not increasing linearly after ~1000 s. This "soak" period ensures that all organic material is removed from the filter before the next collection.
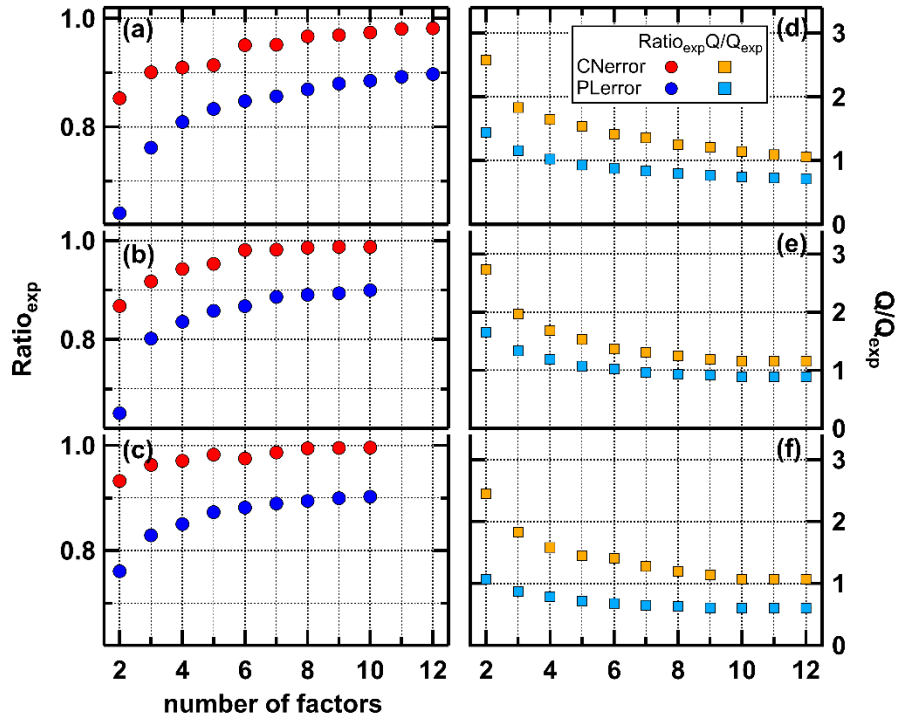
Figure 3: Fraction of explained variance (*Ratio*$_{exp}$, left) and *Q/Q*$_{exp}$ values (right) for the low- (a), medium- (b) and highOC- dataset for PLerror (blue) and CNerror(red).
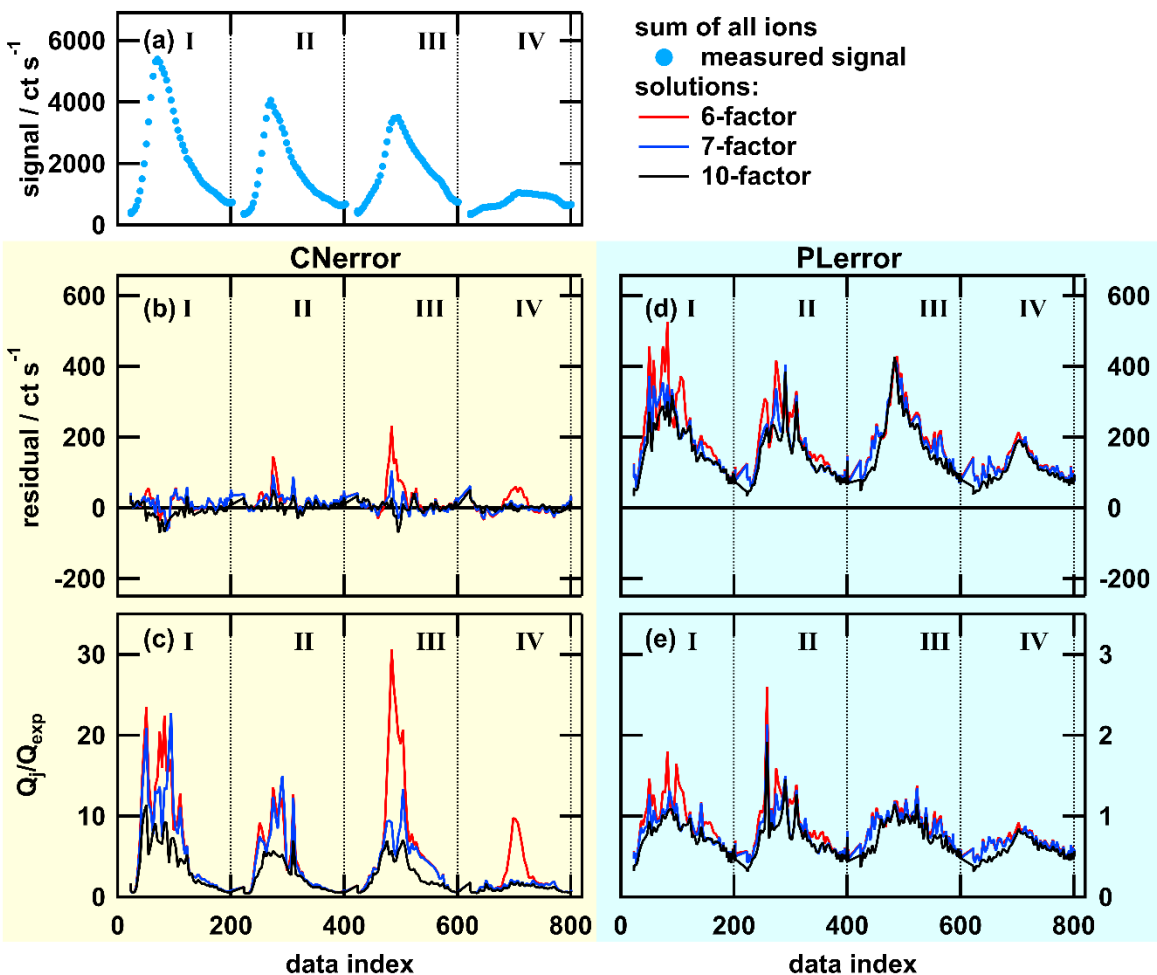
Figure 4: Total ion thermogram (a), residuals (b and d) and Q_j/Q_{exp} values (c and e) as time series for solutions with 6, 7, or 10 factors for PMF run with CNerror (b and c, yellow background) and PLerror (d and e, blue background). The dataset contains thermogram scans for highOC SOA particles of these sampling conditions: dry, $t_{evap} = 0.25$ h (I), dry, $t_{evap} = 4$ h(II), wet, $t_{evap} = 0.25$ h (III), and wet, $t_{evap} = 4$ h (IV). Note that the y scaling is the same in panels (b) and (d), but in (e) it is 10 times smaller than in (c).
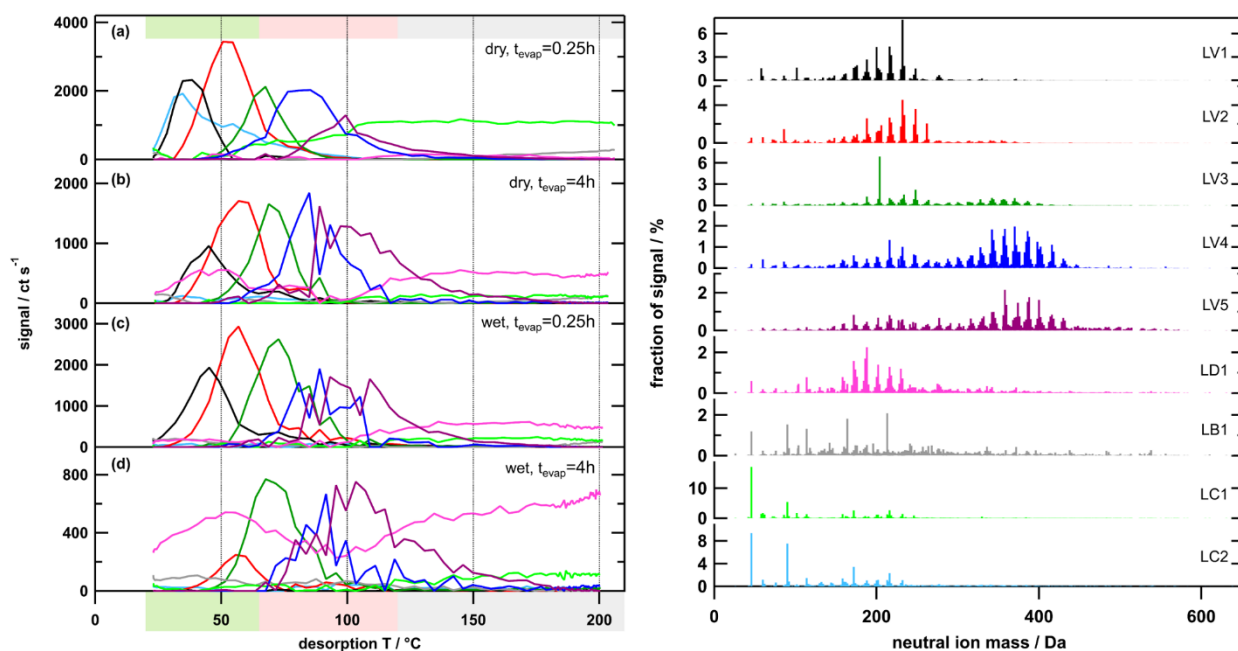
Figure 5: Temperature profiles (left) and factor mass spectra (right) for the 9-factor solution for the lowOC case. Each factor mass spectrum is normalised. The colour code is the same for both panels. Background colours in the left panel indicate volatility classifications according to Donahue et al. (2006) derived from T_{max}-C* calibrations (green: SVOC, red: LVOC, grey: ELVOC). Note the different scaling for y-axes in panels a-d.
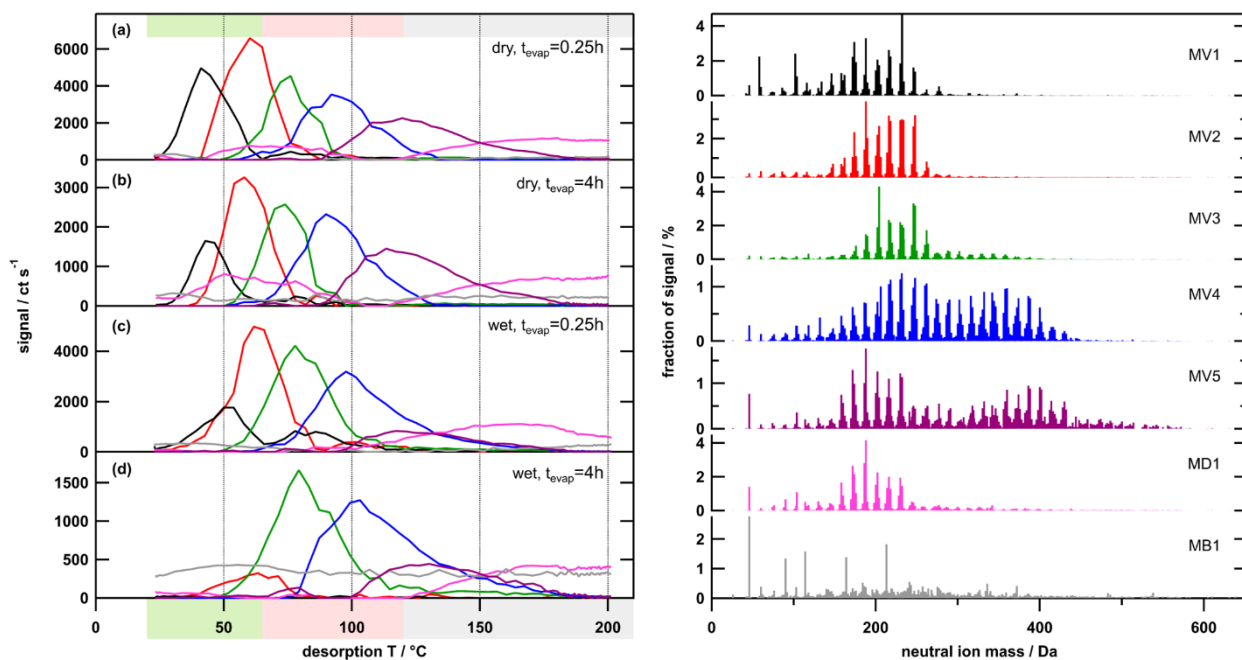
Figure 6: Temperature profiles (left) and factor mass spectra (right) for the 7-factor solution for the mediumOC case. Each factor mass spectrum is normalised. The colour code is the same for both panels. Background colour in the left panel indicates volatility classification derived from T_{max}-C^* calibrations (green: SVOC, red: LVOC, grey: ELVOC). Note the different scaling for y-axes in panels a-d.
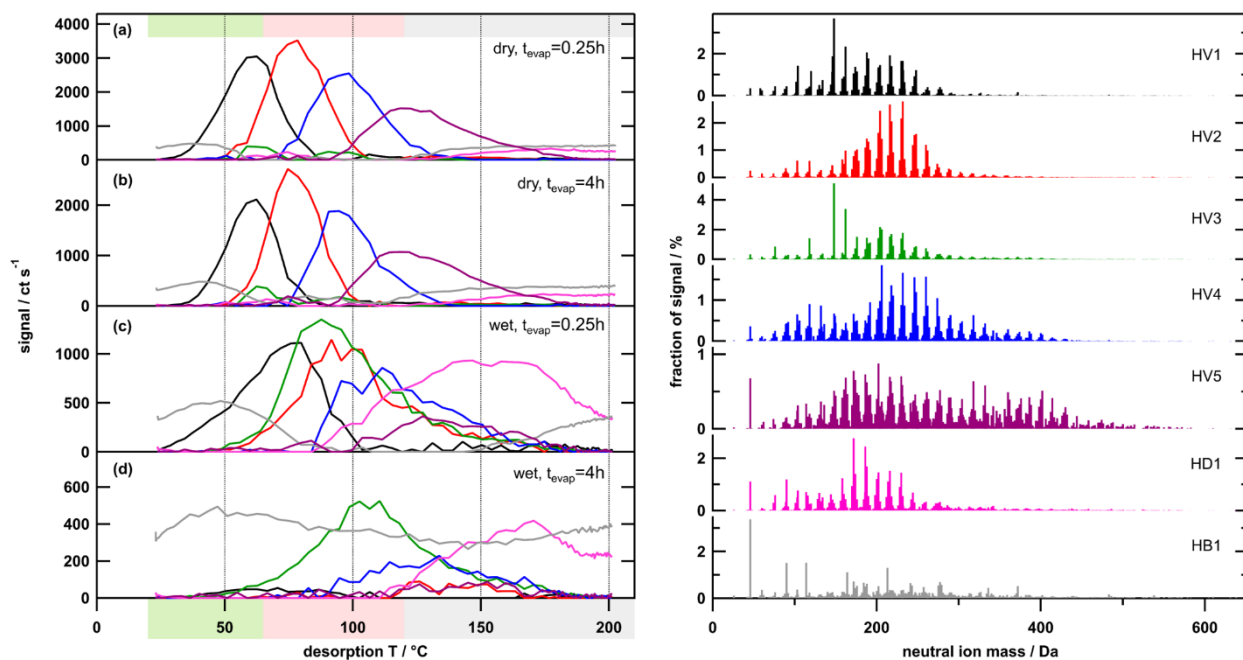
Figure 7: Temperature profiles (left) and factor mass spectra (right) for the 7-factor solution for highOC case. Each factor mass spectrum is normalised. The colour code is the same for both panels Background colour in the left panel indicates volatility classification derived from T_{max} - C^* calibrations (green: SVOC, red: LVOC, grey: ELVOC). Note the different scaling for y-axes in panels a-d.
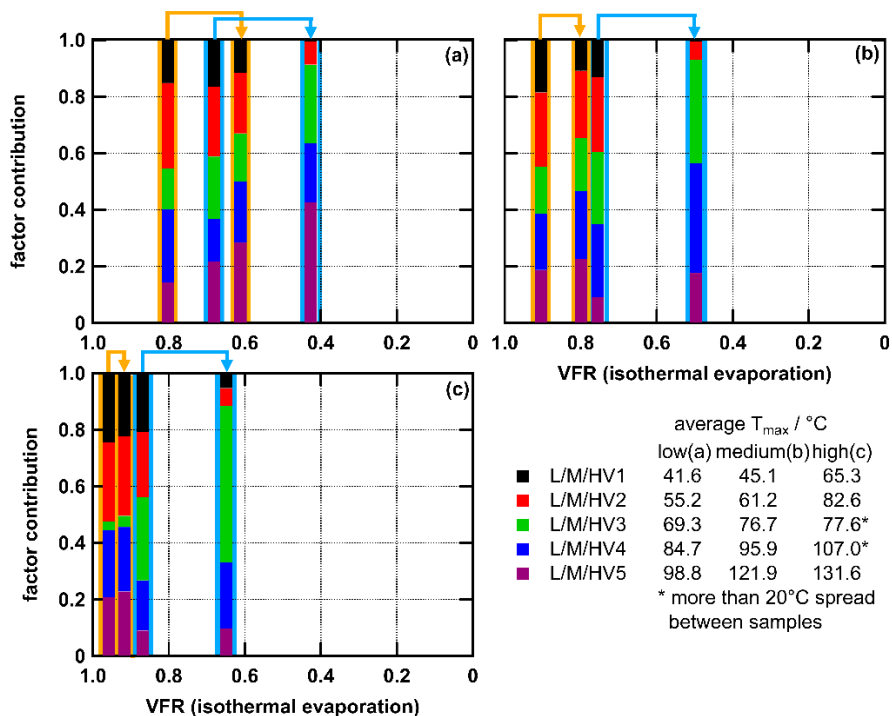
Figure 8: Contribution of type V factors to total signal for low- (a), medium- (b), and highOC cases (c). The x-axis is the average volume fraction remaining (VFR) after comparable time intervals of isothermal evaporation observed measured in separate RTC experiments. Orange and blue arrows indicate the change from $t_{evap} = 0.25$ h to $t_{evap} = 4$ h particles for dry and wet conditions, respectively. Note that the colour code is the same in all panels, but LV1 is not equal to MV1 etc. VFR values are from isothermal evaporation measurements described in Buchholz et al. (2019). Average T_{max} values are for comparison of the volatility of the factors. Detailed values are given in Table 2.
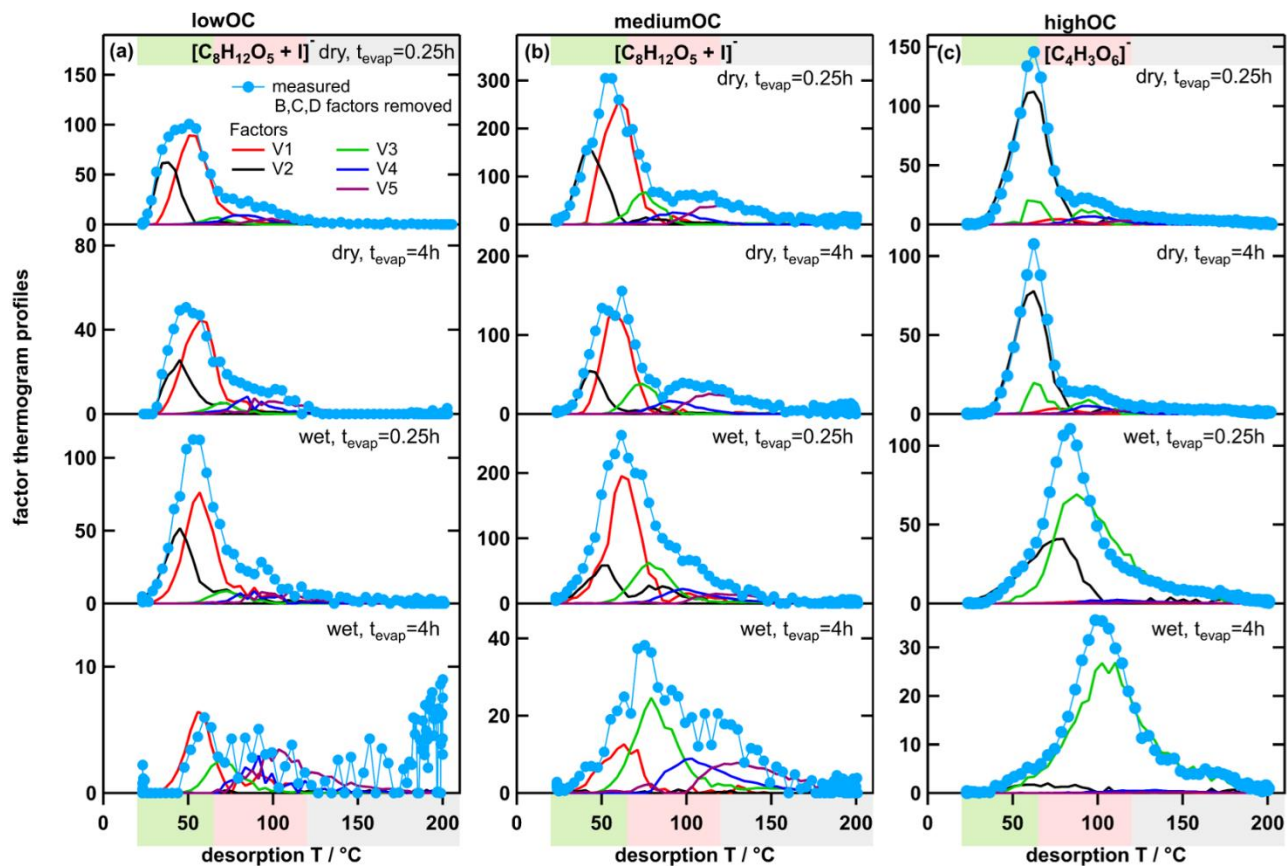
Figure 9: Measured ion thermograms and factor thermogram profiles for ion $[C_8H_{12}O_5+I]^-$ in the low- (a) and mediumOC cases (b) and $C_4H_3O_6^-$ in the highOC case (c). Note that to reduce clutter in the graph only V-type factors are displayed. Thus, coloured lines will not add up to the measured values (light blue) if the sample to background ratio was low (e.g. bottom panel in a).
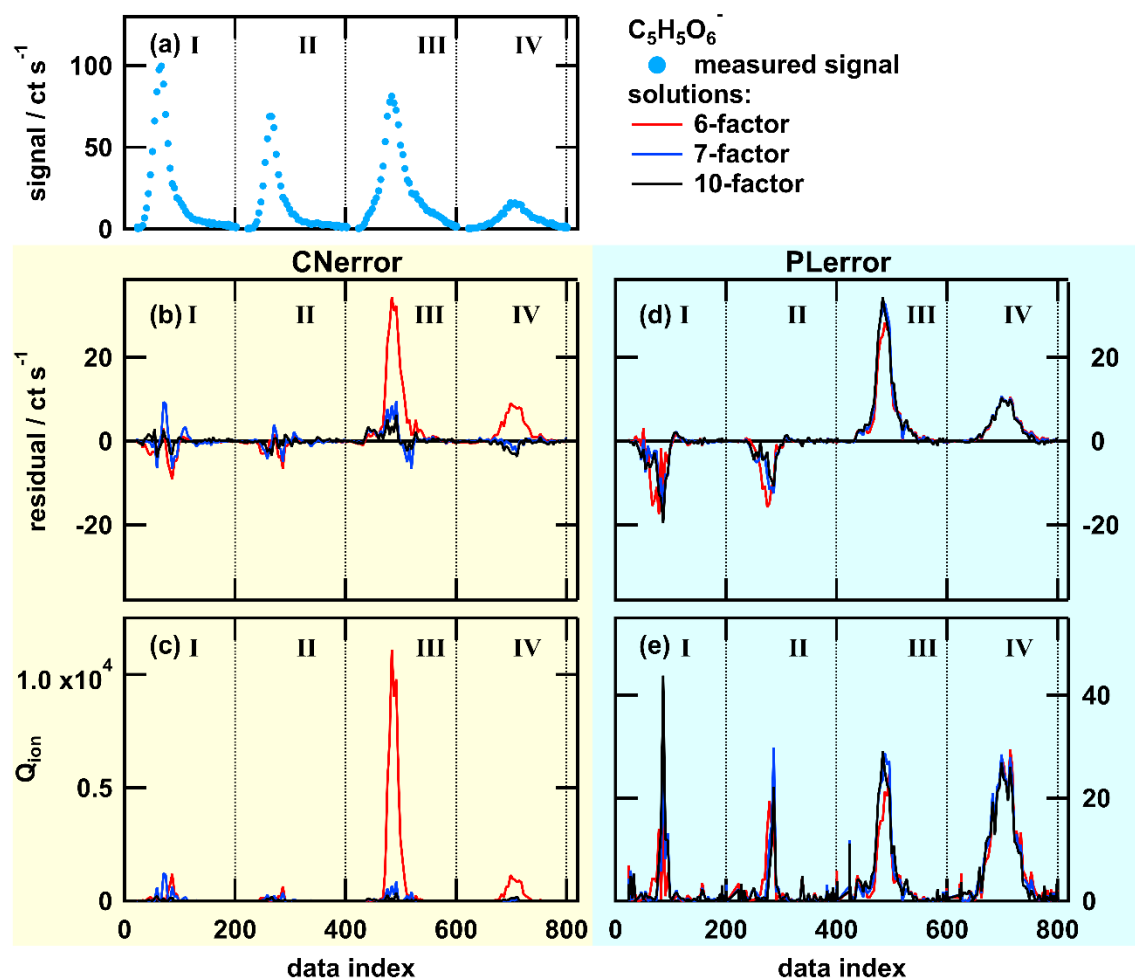
Figure A 1: Single ion thermogram (a), residual (b and d), and Q_{ion} values (c and e) as time series for solutions with 6, 7, or 10 factors for PMF run with CNerror (b and c) and PLerror (d and e) for the ion $C_5H_5O_6^-$. The dataset contains thermogram scans for highOC SOA particles of these sampling conditions: dry, $t_{evap} = 0.25$ h (I), dry, $t_{evap} = 4$ (II), wet, $t_{evap} = 0.25$ h (III), and wet, $t_{evap} = 4$ h (IV). Note that the y scaling is the same in panels (b) and (d) but in (e) it is much smaller than in (c).
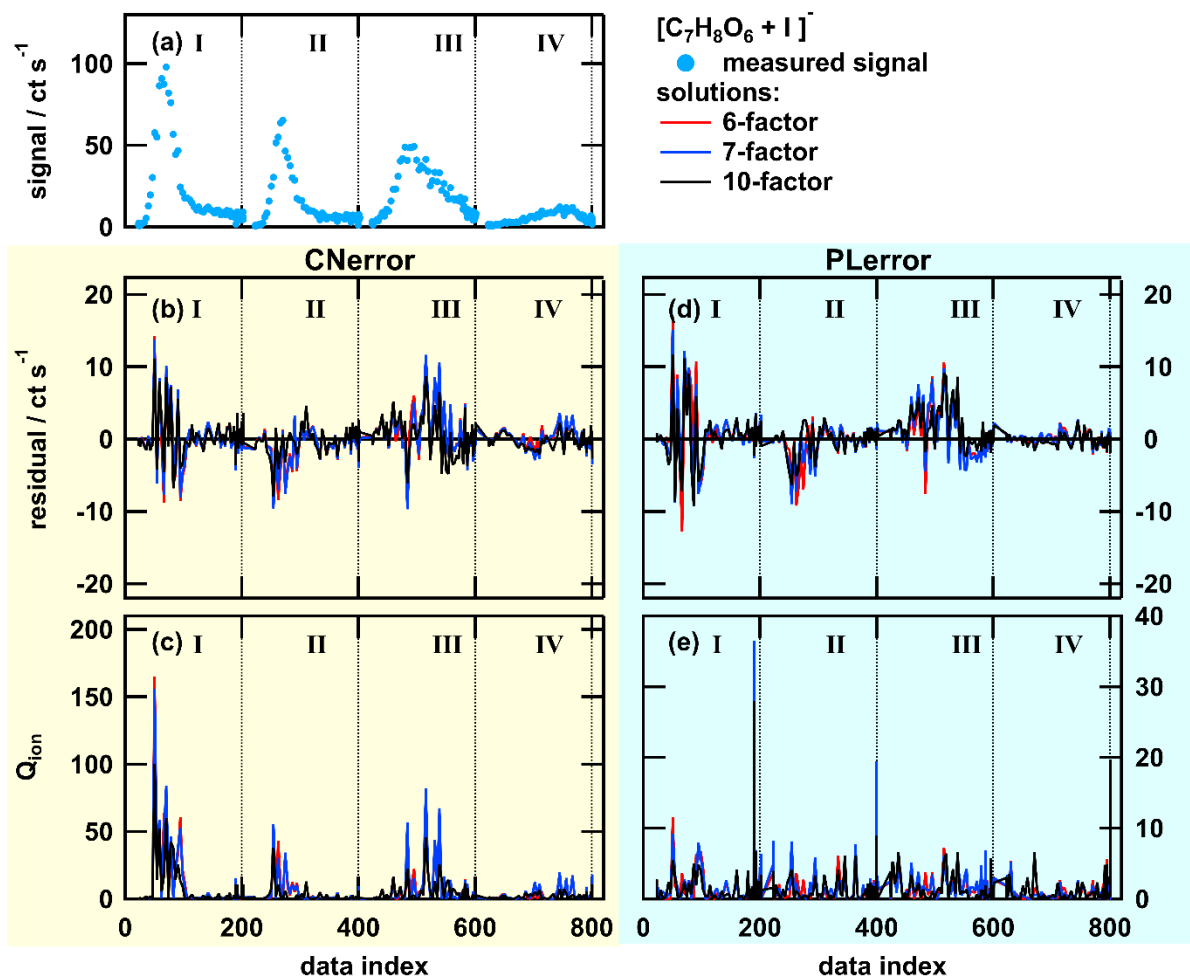
Figure A 2: Single ion thermogram (a), residuals (b and d), and Q_{ion} values (c and e) as time series for solutions with 6, 7, or 10 factors for PMF run with CNerror (b and c) and PLerror (d and e) for the ion $[C_7H_8O_6 + I]^-$. The dataset contains thermogram scans for highOC SOA particles of these sampling conditions: dry, $t_{evap} = 0.25$ h (I), dry, $t_{evap} = 4$ h (II), wet, $t_{evap} = 0.25$ h (III), and wet, $t_{evap} = 4$ h (IV). Note that the y scaling in (e) is much smaller than in (c).
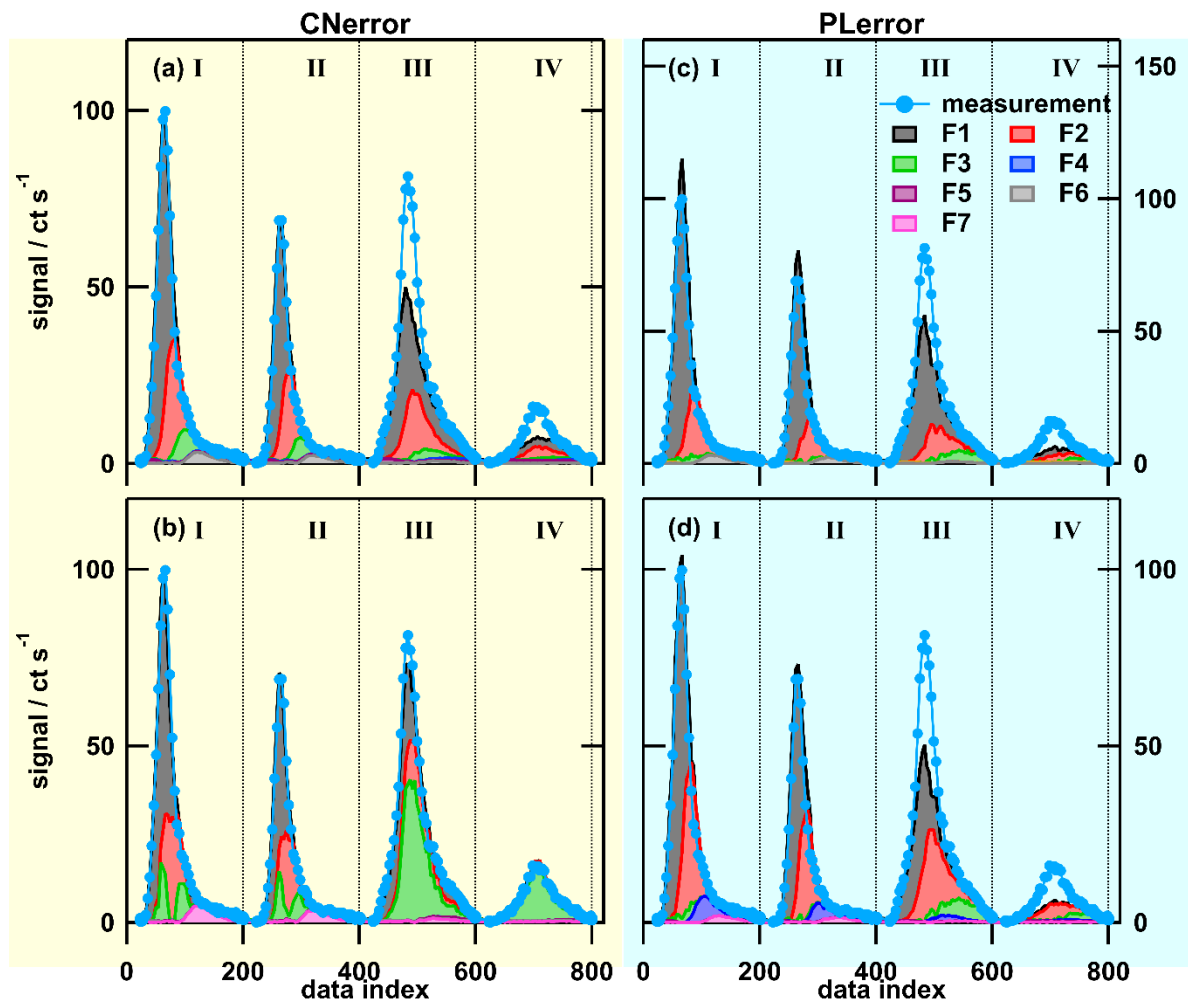
Figure A 3: Combined single ion thermograms of the ion $C_5H_5O_6^-$ for PMF factor profiles for 6 (a and c) and 7 (b and d) factor solution. Left column (a and b) are calculated with CNerror, right column (c and d) with PLerror. The dataset contains thermogram scans for highOC SOA particles of these sampling conditions: dry, $t_{evap} = 0.25$ h (I), dry, $t_{evap} = 4$ h (II), wet, $t_{evap} = 0.25$ h (III), and wet, $t_{evap} = 4$ h (IV). Note that generally the factors are not the same between the two error schemes or the two solutions (i.e., F1 in the 6-factor solution with CNerror is different from F1 in the 7-factor solution with CNerror etc.)